**The Thesis Committee for David Seiji Kar Liang Choi**
**Certifies that this is the approved version of the following thesis:**

# Nanoparticle Characterization with Nanopore Sensors

**APPROVED BY**
**SUPERVISING COMMITTEE:**

**Supervisor:**

Li Shi

S.V. Sreenivasan

# Nanoparticle Characterization with Nanopore Sensors

**by**

**David Seiji Kar Liang Choi, B.S.**

**Thesis**

Presented to the Faculty of the Graduate School of

The University of Texas at Austin

in Partial Fulfillment

of the Requirements

for the Degree of

**Master of Science in Engineering**

**The University of Texas at Austin**

**August 2014**

# Abstract

## Nanoparticle Characterization with Nanopore Sensors

David Seiji Kar Liang Choi, M.S.E.

The University of Texas at Austin, 2014

Supervisor: Li Shi

A silicon nitride, solid-state nanopore sensor for characterizing nanoparticles suspended in an aqueous medium is presented, and the fundamental theory of resistive-pulse sensing based on the Coulter principle is derived. Careful analytical and experimental considerations in the interrelationships between the electrolyte concentration, nanoparticles, applied bias voltage and electronic equipment are described in detail. Various electromagnetc noise sources present in low-current electrochemical experiments are identified and eliminated. Finally, 100 nm charged polystyrene beads are analyzed by pores ranging in diameter from 300 – 500 nm. The experimental results are found to be in good agreement with the expected event depths and event durations as described by mathematical models found in the literature.

# Table of Contents

# Chapter 1: Introduction

## 1.1 Nanoparticles as an Emergent Biomedical Technology

Nanotechnology has long been a subject of high interest as the key to a virtually unlimited frontier of scientific discovery. Since Feynman's speech "There's Plenty of Room at the Bottom" at Caltech in 1959, the manufacturing of micro and nano-scale devices has been inexhaustible and is accompanied by an even larger breadth of applications. Beyond academia, these "invisible" tools have enabled groundbreaking advancements in disciplines ranging from computer science to environmental safety and more recently in the realm of life sciences [1-4]. In particular, the unique properties of nanoparticles from their bulk counterparts has propelled researchers' interest in their use as both biological diagnostic tools as well as more efficient drug delivery agents [3-9]. Their characteristic dimensions, for example, allow them to interact with biological samples at a sub-cellular level that is unachievable at larger scales [3]. In one principally emergent field, nanoparticles have been imagined to replace traditional chemotherapy as a more efficacious method in treating patients diagnosed with cancer. The leaky vasculature surrounding tumors is caused by a phenomenon called the Enhanced Permeability and Retention (EPR) effect [11]. Owing only to their size, nanoparticles are more readily able to navigate across this vasculature and accumulate in and around tumors. In a related publication, Agarwal, et. al., showed that mammalian cells preferentially uptake particles of a certain geometry [10]. Furthermore, nanoparticles can

be made to actively target certain biological entities by engineering them with specific surface moieties and a deliberate drug release mechanism [3]. The ability to create a so-called "smart" drug with a high degree of biological specificity has therefore become the driving force behind nanoparticle development in the biomedical field.

## 1.2 Nanoparticle Characterization

Before a drug is approved for human trials, the Food and Drug Administration (FDA) requires that it be tested for biocompatibility, immunotoxicity, purity, and sterility [3]. In the context of nanoparticles, these drug characteristics in turn depend on their physical size, shape, surface charge, and the distribution of these properties in a given population. As a relatively new technology, nanoparticle development and their characterization are not well-founded practices and lack standardized metrology methods for quality control. Two currently widely adopted methods to characterize particles are the Dynamic Light Scattering (DLS) and Scanning Electron Microscopy (SEM) techniques.

### 1.2.1 Dynamic Light Scattering

As its name suggests, DLS is a technique based on the light scattering properties of particulates (the analyte) suspended in an aqueous media and has been used extensively to determine the size and charge of a population of nanoparticles in solution [12-19] . Commercially available systems pass a monochromatic light through a cuvette containing a dilute suspension of the analyte of interest. A detector at a fixed angle

relative to the light source monitors the time-dependent scattering intensity. An autocorrelation function is then fit to the intensity fluctuations and is used to determine the average diffusion coefficient of the particles as they move under Brownian motion. The Stokes-Einstein relation is then applied to relate the population averaged diffusion coefficient to a corresponding population averaged hydrodynamic particle diameter [15]. In a similar manner, when an electric potential bias is applied to the cuvette, an average electrophoretic mobility of the suspended particles can be determined. From this, the particles' surface charge can be assessed.

While it is an established and easy-to-use method, DLS has two critical pitfalls. First, it provides a population averaged particle size and does not measure particles on an individual basis. Furthermore, the Stokes-Einstein equation is only valid for spherically shaped particles and does not give information on any other geometry. As a result, solutions containing a range of particle sizes and shapes will produce a single averaged hydrodynamic diameter, ignoring important geometric property distributions. While the method is highly effective in characterizing a monodisperse population of spherical particles, its theoretical operating principle is limited in flexibility and applicability to the more diversified suspensions required for nanoparticle drug carriers.

### 1.2.2 SEM and AFM

A second widely adopted technique in particle characterization is direct visualization using an SEM and indirect topology scanning using AFM [20-24]. While these methods are able to directly measure the size and shape of individual nanoparticles,

they are restrictively slow in measuring large populations. Measurement tests of even a few hundred particles can be orders of magnitude longer than an analysis using DLS, which takes only a matter of minutes. In addition, SEM and AFM measurements are usually done on dry samples. Particles cannot be measured in their native, aqueous environment. Therefore, these techniques are unable to provide information on particle aggregation, ζ-potential, and swelling of particles within solution.

Although easy to use and well-established, the DLS, SEM and AFM characterization techniques are ill-equipped to fully describe the diverse nature of nanoparticles used in biomedical applications. As a result, a more flexible measurement platform is required. The development of such a system based on the resistive-pulse method is the focus of this thesis.

### 1.3 Nanopore Based Resistive-Pulse Sensing

Nanopore sensing has solicited an enormous amount of research interest in the past decade for its potential in characterizing inorganic particles, organic molecules, living cells, and DNA sequencing [25]. The working principle of all pore sensors is based on the original patent by Walter Coulter, who invented the technique to count particles suspended in a fluid [26]. The method is relatively simple and is based on electrically detecting the passage of a particle through an aperture of similar, but larger diameter. A pore embedded in a membrane is used to separate two chambers, referred as cis-chamber and trans-chamber, each filled with electrolyte solution. The cis-chamber initially contains a suspension of the analyte of interest and the trans-chamber initially

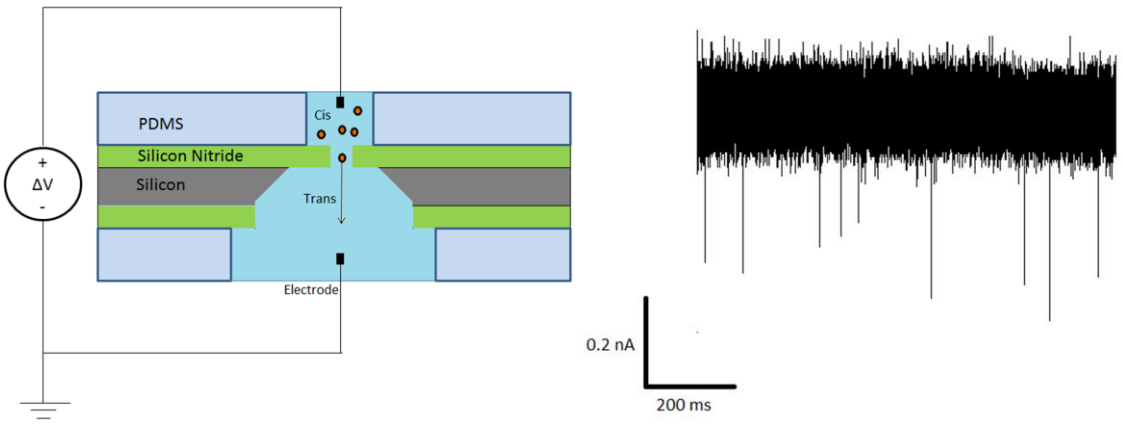


Figure 1: a.) Basic schematic of a nanopore sensor. An electric potential bias is applied between two electrolyte filled chambers separated only by a nanopore in a suspended silicon nitride membrane. Particles travel from the cis to trans chamber toward the oppositely charged electrode (particles are positively charged in this depiction) b.) Typical current trace during particle translocation events.

contains only the suspending medium. Electrodes are inserted into each chamber and an electric potential is applied, simultaneously generating an ionic current through the pore [27]. As particles travel from the cis to trans chambers, they displace a finite volume of ionic solution within the pore. As a result, the measured ionic current temporarily decreases during the translocation, and returns to its baseline value after the particle has completely exited the aperture. Useful information about the particle can be gathered by close examination of the electrical signal. The magnitude of the current drop, for instance, is indicative of the size of the particle as it is related to the volume of ionic solution excluded by the particle's presence within the pore. When driven by an electric field gradient, the duration of the translocation event can be used to determine the effective surface charge of the particle and the shape of the current pulse is representative of its geometry [28-31]. In general, the technique is fast (10s to 100s of events/s), measurements are done in a more natural aqueous environment, and analyses are

performed on a particle by particle basis. To this end, nanopore sensors show a greater promise over DLS, SEM or AFM as a metrology tool and quality control technique for characterizing populations of nanoparticles as drug delivery agents. Figure 1 shows the basic components and a typical signal in nanopore experiments.

Beyond particle characterizations, nanopore sensors show a greater breadth of application in the detection and analysis of a plethora of biological molecules [13, 15, 19, 22, 28, 29, 32, 42, 55, 60, 70]. Size, shape, and charge specific viruses and bacteria may be probed allowing for pore sensors to be used as air and water pollutant detectors or as early diagnostic tools. In a similar manner, they can be employed as hazardous biological agent sensors for military application. The most prominent potential for such sensors, however, is the allure of DNA sequencing in a simple, cheap, and fast platform, which has captivated the attention of many research groups in both academia and industrial settings [33-39]. Successful and affordable sequencing of the human DNA promises to transform modern medicine, whereby preventative and patient-specific medical treatments can be tailored to an individual's unique genetic makeup. Distinct detection of each of the four DNA base nucleotides, Adenine, Guanine, Cytosine, and Thymine, has been shown to be feasible in biological nanopore sensors [40]. While biological pores are highly reproducible, exhibit low electronic noise characteristics, and are on the size scale conducive to DNA sequencing, they are very unstable in all but a small range of experimental conditions. For example, the pH of the electrolyte solution must be maintained within a narrow range of biologically relevant values, and the lipid bilayer

membrane in which the pores must be embedded lacks thermal, electrical and mechanical stability [41]. Due to advancements in micro and nano-fabrication technologies, solid-state pores have become common place in nanopore sensors. While they typically exhibit worse electrical noise properties, synthetic pores are robust, can be chemically modified, and are easily manufactured in a large range of diameters allowing for the analysis of a wider selection of analyte sizes. Continuing research in the field of direct ionic conductance measurements for sequencing DNA has shown that identification of individual bases is possible, though it has not yet been achieved [41]. As a result, pores fabricated in solid-state silicon nitride membranes were chosen in the present experiments because of their robustness and far-reaching potential in drug and DNA assay applications.

Nanoparticle detection using the resistive-pulse method is a difficult process requiring fundamental understandings of electronics engineering, materials science, electrochemistry, colloidal particle theories, and surface sciences [41]. This thesis presents the foundation of nanopore experiments and describes in detail the necessary key concepts and considerations in the development of a working system. Beginning with the theoretical background of conductance measurements of a nanopore in electrolyte solution, this thesis provides extensive discussions on the necessary system specifications, fabrication techniques, and subtle interplay between experimental parameters that are not described in the literature. Finally, experimental data of 100 nm polystyrene particles is presented and compared to published theoretical models as a

proof of concept. The final system is envisioned to enable exploration of the shape characteristics of nanoparticles, a novel use of the established method.

# Chapter 2: Nanopore Theory

A fundamental understanding of charged-species transport is the foundation of all nanopore sensors. When exposed to an electric field, the flow of ions through a pore dictates the magnitude of the electrical current. Likewise, the charged nature of particles in solution governs their motion and behavior as they travel through a pore under the influence of an electric field. Together, these two concepts form the basis of nanopore sensing and determine the overall signal and noise characteristics of an experiment. Therefore, the aim of this chapter is to develop the relationships between electric fields, charged species, and synthetic nanopores in fluidic environments.

## 2.1 Conductance of a Long, Narrow, Cylindrical and Uncharged Channel

Nanopore sensing is a complex problem involving fluid dynamics, mass transfer, and electrostatic fields. In general, this requires simultaneously solving the Navier-Stokes, Nernst-Plank, and Poisson equations for the fluid flow field, ion flux, and charge distribution, respectively. We begin with expressions for the diffusively and electrophoretically driven flux, M, of an ionic species, i:

$$M_i = M_i^{diff} + M_i^{elect} \tag{2.1}$$

$$M_i = -D_i \frac{dc_i}{dx} - \mu_i c_i \frac{d\varphi}{dx} \tag{2.2}$$

where $D_i$ , $c_i$, and $\mu_i$ are the diffusion coefficient, concentration, and electrical mobility of species i, respectively, and $\phi$ is the local electric potential. Note that, in general, a pressure gradient may also be applied across the nanopore to enhance translocation

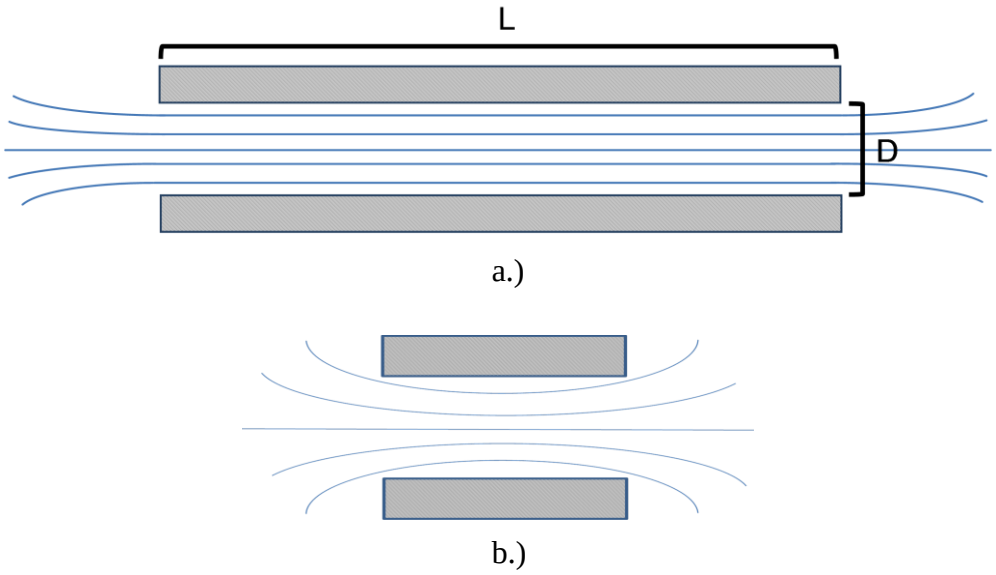


Figure 2: a.) Parallel electric field lines in a high aspect ratio pore b.) Depiction of a low aspect ratio pore with curving field lines near the entrance and exit (Exaggerated within the pore for emphasis).

events [42], but within the scope of the present experiment this flux term was equal to zero. Here we also assume a constant and unidirectional electric field, which may not necessarily be the case in some situations and will be addressed later (Figure 2). For dilute electrolyte solutions, the electrical mobility, μ, can be related to the diffusion coefficient by the Nernst-Einstein relationship [43]:

$$D_i = \frac{\mu_i k_b T}{q} \tag{2.3}$$

where $k_b$ is the Boltzmann's constant, T is temperature, and q is the electrical charge of species i. Equation 2.3 can be simplified into a more convenient and familiar form by using the relations:

$$k_b = \frac{R}{N_a} \tag{2.4}$$

$$q = z_i \cdot e \tag{2.5}$$

$$F = e \cdot N_a \tag{2.6}$$

where R is the universal gas constant, $N_a$ is Avagadro's number, F is Faraday's constant, $z_i$ is the valence of ionic species i, and e is an elementary charge. Substituting equations 2.4-2.6 into equation 2.3 and then substituting into equation 2.2, we arrive at the molar flux of ionic species i as a function of its concentration, diffusivity, and an electric field gradient:

$$M_i = -D_i \frac{dc_i}{dx} - c_i \frac{D_i z_i F}{RT} \frac{d\varphi}{dx} \tag{2.7}$$

Equation 2.7 is a familiar form of the Nernst-Planck equation which governs ionic species transport under a concentration gradient (first term, i.e. Fick's first law) and electric field gradient (second term). The ionic current density can then be obtained from the molar flux by multiplication by the valence and Faraday's constant and summing over all ionic species:

$$J = F \cdot \sum_i z_i \cdot M_i \tag{2.8}$$

For a 1:1 ionic solution such as the KCl used in the experiments, $c_{K+} = c_{Cl-} = c$ and $z_{K+} = -z_{Cl-}$ and equation 2.8 becomes:

$$J = -\frac{z^2 F^2}{RT} \cdot [D_{K+} + D_{Cl-}] \cdot c \cdot \frac{d\varphi}{dx} \tag{2.9}$$

where the diffusive terms have been dropped since the concentrations are equal on either side of the membrane (i.e. ion transport is due only to the applied electric field). The units of $J$ are $\left[\frac{A}{m^2}\right]$. Equation 2.9 can be written in more compact form as [14]:

$$\frac{z^2F^2}{RT} \cdot (D_{K+} + D_{Cl-}) \cdot c = \sigma_s$$

$$-\frac{d\varphi}{dx} = E$$

$$J = \sigma_s \cdot E \tag{2.10}$$

for $\sigma_s$ as the bulk solution conductivity and the electric field, E. In the case of a long, straight, and narrow channel (i.e. L/D >> 1) as in figure 2a, the electric field lines are parallel and the electric field E is constant:

$$E \cong \frac{\Delta V_{pore}}{L} \tag{2.11}$$

where $\Delta V_{pore}$ is the voltage across the nanopore and L is the length of the pore. As we will discuss in later sections, $\Delta V_{pore} = \Delta V_{applied}$ only in the ideal case where the pore resistance is the dominating resistance. The total ionic current flowing through the pore is then found by multiplying the ionic current density, $J$, by the cross sectional area of the pore:

$$I = \sigma_s \cdot \frac{\Delta V_{pore}}{L} \cdot A_{pore} = \frac{\pi D^2}{4L} \cdot \sigma_s \cdot \Delta V_{pore} \tag{2.12}$$

From which the theoretical conductance of the pore can be derived:

$$G_{pore} = \frac{I}{\Delta V_{pore}} = \sigma_s \cdot \frac{\pi D^2}{4L} \tag{2.13}$$

Therefore, we have derived the conductance of a nanopore from basic principles. The result is elegant and unsurprising. It is the same relation for a solid resistor (i.e. conductivity x Area ÷ Length) and is therefore conceptually identical to a "fluidic wire" where the ionic solution fills the nanopore cross section. This relatively simple model,

which assumes a constant pore cross section, parallel electric field lines (L>>D), and an uncharged pore surface, is a great place to begin nanopore theory as it provides a compact, analytical expression with physical insight into some of the relevant parameters. The following sections discuss deviations from this ideal model and assess their relevant significance in the physical system under study [41, 44].

## 2.2 Effect of access resistance

In the previous derivation of pore conductance, a high aspect ratio pore (L/D >> 1) was considered. This allowed for the assumption of parallel electric field lines within the pore and negligible effects of curved field lines at the entrance and exit of the pore (figure 2a and b). However, in many practical situations L/D is on the order of 1 or less and the end effects of the pore must be considered as additional series resistances with the pore (figure 2b). This so called "access resistance" is analogous to the "spreading resistance" around a point contact [41]. A theoretical model presented by Hille treats the ends of the pore as half hemispherical regions that extend into the bulk solution. Hille treated the access resistances as the convergence resistance to a hemisphere and approximated:

$$R_{access}^{Hille} = \frac{\rho_s}{\pi r} \tag{2.14}$$

for bulk solution resistivity $\rho_s$ and pore radius r. This approximation neglects the effects *within* the hemisphere around the pore, however, and was more accurately accounted for later by Hall. Hall's model is based on the resistance between a hemispherical electrode

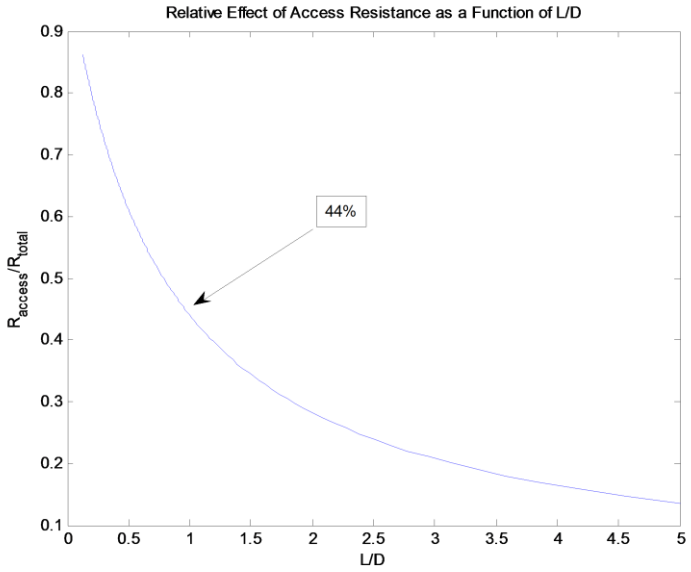


Figure 3: Relative effect of access resistance as a function of aspect ratio.

at an infinite distance from a flat circular disk, which represents the entrance to the pore. Hall argued that the resistance between these two electrodes in a conducting medium is related to the capacitance of the two electrodes when separated by a dielectric:

$$R_{access}^{Hall} = \frac{\varepsilon \rho_s}{C} \tag{2.15}$$

where ε is the permittivity of the dielectric and C is the capacitance of the two electrode system. Using a well known solution for the capacitance of a hemispherical electrode to a circular disk electrode, Hall then solved for the access resistance exactly:

$$C = 2\varepsilon D \tag{2.16}$$

$$R_{access}^{Hall} = \frac{1}{\sigma_s D} \tag{2.17}$$

where $\sigma_s$ and D are the conductivity of the bulk solution and pore diameter, respectively. The given result in equation 2.17 was multiplied by a factor of 2 to account for access resistances on both sides of the pore.

The access resistance is in series with the pore resistance given by the inverse of equation 2.13. Therefore the total resistance of the system is summation of the two:

$$R_{total} = \frac{1}{\sigma_s}\left(\frac{4L}{\pi D^2} + \frac{1}{D}\right) \tag{2.18}$$

Figure 3 shows a plot of the relative significance of the access resistance as a function of the aspect ratio of the pore. As predicted, the relative effect of the access resistance decreases as the aspect ratio L/D increases, and the solution converges to equation 2.13 there. In the experiments that were conducted, the L/D ratios ranged from approximately 0.6 to 1. Referring to figure 3 the access resistance for these ratios is approximately 44-50% of the total resistance and contributes a significant amount to the total resistance. The access resistance is affected only by the regimes within a few pore diameter away from the pore, as the potential follows a 1/r dependence and quickly approaches the electrode potential at a few diameters away from the pore.

In general, this large access resistance contribution has implications in choosing the correct experimental parameters, such as the voltage bias, as well as in the analysis of the translocation signal. These ramifications will be discussed in more detail after a basic theory of signal analysis is presented, but at this point it suffices to say that the access resistance is a non-negligible parameter that must be properly assessed.

## 2.3 Surface Charge, Zeta-Potential, EDL, and Debye Length

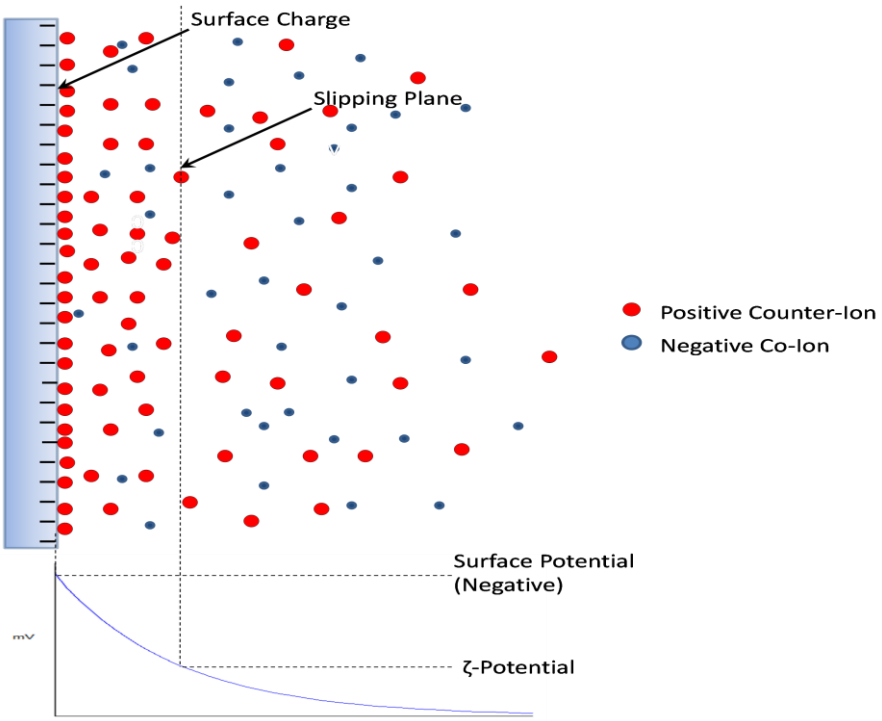


Figure 4: Schematic of a charged particle in ionic solution with surrounding electric double layer. Counter-ions within the dashed line are immobilized due to strong electrostatic attractions. Outside of the slipping plane, counter-ions are free to move relative to the particle surface. The effective electric potential at the slipping plane is defined as the ζ-potential of the particle.

Another possible deviation from the previous pore conductance model is the effect of surface charges on the pore. Before this is discussed, it is important to understand the charged nature of solid surfaces in ionic solution as it pertains to both the pore conductance as well as the target particles of interest.

Nearly all surfaces obtain a finite charge when submersed in an aqueous medium. This charge could result from a number of different phenomena depending on the material. In many cases, the charge is a result of ionization of surface functionalities

such as the ionization of –COOH groups, as is the case with the nanoparticles used in this experiment [41]. The degree of ionization is dependent on several factors including the solution pH, electrolyte concentration and temperature [16, 17, 30, 47, 48]. In most situations much of this surface charge is shielded by the oppositely-charged free-ions ("counter-ions") in the solution, which are electrostatically attracted to the surface. Along the same lines, like-charged ions ("co-ions") are repelled. The electric potential at a defined distance away from the surface (vide infra) caused by the left-over effective charge is referred to as the ζ-potential and is a fundamental parameter in pore studies.

Figure 4 shows a schematic view of a charged surface in ionic solution. For a negatively charged surface, positively charged counter-ions in the solution are attracted. The strong electrostatic attraction of the ions in closest contact with the surface immobilizes them, neutralizing some of the charge. This process continues as one moves further away from the surface and into the bulk solution, which results in an exponentially decreasing electric potential as a function of distance until charge neutrality is met far from the surface. As more counter-ions continue to shield the surface charge, the electrostatic force exerted on them weakens. At some distance away, while there is still an excess of counter-ions and local charge neutrality is not yet met, the counter-ions are only weakly attracted to the surface and are no longer bound but can be sheared away by Brownian motion [49]. This imaginary plane which separates the immobilized counter-ions from the cloud of excess and freely moving counter-ions is called the slipping plane. This structure is commonly known as the electric double layer, or EDL,

where the first layer consists of immobilized ions on the surface and the second layer consists of a concentrated cloud of mobile counter-ions with co-ions sporadically dispersed throughout. The electric potential at the boundary between the two layers is the ζ-potential, i.e. caused by the effective charge of the surface [49]. An approximation of the thickness of a double layer can be found by finding the distance away from the surface at which the electrical potential energy balances the thermal (Brownian) motion energy. We first assume a locally flat surface whereby the electric field is parallel to the normal to the surface. For simplicity, we also assume that there are no co-ions present in the EDL and the concentration of counter-ions is constant throughout the EDL. The work required to move a charge along a length x is:

$$\Delta w = \frac{Fz^2cx^2}{2\varepsilon} \tag{2.19}$$

Balancing this electrostatic potential energy change with the thermal motion energy we obtain:

$$\frac{Fz^2cx^2}{2\varepsilon} = RT$$

$$x \equiv \lambda_d = \sqrt{\frac{2\varepsilon RT}{F^2z^2c}} \tag{2.20}$$

where $\lambda_d$ is defined as the Debye shielding length and all other parameters are as previously defined. While this is a simple approximation, charge neutrality can

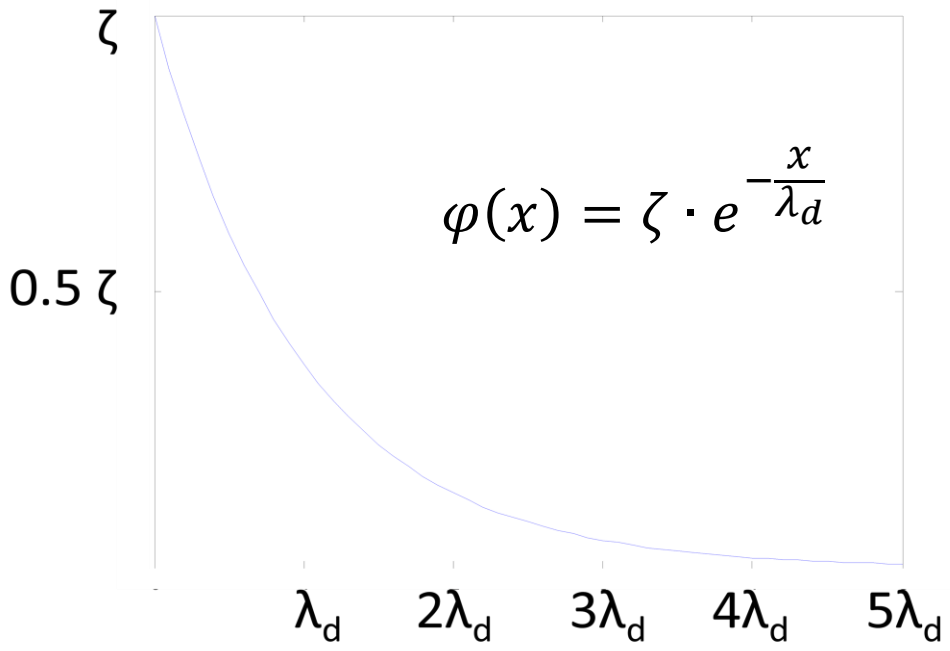


Figure 5: Electric potential as a function of distance from slipping plane.

reasonably be assumed at 2-3 $\lambda_d$ distances from the surface in most cases. A more complicated solution was presented by Debye and Huckel, which accounts for a non-uniform counter-ion distribution within the EDL and is derived here to show the effect of the surface charge as a function of distance from the surface. They assume the concentration of ions in the layer has a Boltzmann distribution:

$$c_+(x) = c_o \exp\left(\frac{-Fz\varphi(x)}{RT}\right) \tag{2.21}$$

where $c_o$ is the concentration of counter-ions in the bulk solution. Furthermore, Poisson's equation for the electric potential as a function of x can be stated as:

$$\frac{d^2\varphi}{dx^2} = -\frac{\rho_e(x)}{\varepsilon} \tag{2.22}$$

where $\rho_e$ is the space charge density in the double layer and is related to the concentration distribution of counter-ions by:

$$\rho_e(x) = F \sum_i z_i c_i(x) \tag{2.23}$$

Substituting 21 and 23 into 22 yields a rather complex second order differential equation [50]:

$$\frac{d^2\varphi}{dx^2} = -\frac{F}{\varepsilon}\sum_i z_i c_{i_o} \exp\left(-\frac{F z_i \varphi}{RT}\right) \tag{2.24}$$

Solving for equation 2.24 is non-trivial. Bagotsky, et. al., has offered a detailed mathematical solution of equation 2.24, and reported the final result as:

$$\varphi(x) = \varphi_o \exp\left(-\frac{x}{\lambda_d}\right) \tag{2.25}$$

for the boundary conditions $\phi(x=0) = \zeta$ and $\phi(x=\infty) = 0$, i.e. the solution is valid in the region from the slipping plane where the potential is equal to the $\zeta$-potential to the bulk solution where electro-neutrality is satisfied. Equation 2.25 is plotted in figure 5. Notice that after several Debye lengths, $\lambda_d$, the effects of the surface charge are neutralized by the attracted counter-ions. Therefore $\lambda_d$ is an appropriate length scale when describing the extent to which surface charge is significant.

As a summary, this section qualitatively and quantitatively discussed the concept of surface charge, zeta-potential (i.e. the effective potential after counter-ion shielding), electric double layer (EDL), and double layer thickness (i.e. the extent to which the surface charge is felt). These concepts and definitions will be invaluable in the coming

discussions on electrophoresis, electroosmosis, nanoparticle stabilization, signal analysis, and charged pore conductances [49].

## 2.4 Effect of charged pore

Another simplifying assumption that was made in the previous derivation of pore conductance was that of a pore with uncharged inner surfaces. This allowed us to treat the ion distribution inside the pore as the bulk concentration. As was discussed in the previous section, most solid surfaces exposed to a liquid environment attain a finite surface charge, which changes the local ion distribution. More specifically, there is a greater concentration of counter-ions near the solid surface to balance its intrinsic charge and electroneutrality is no longer valid. When an electric bias is applied, an additional ionic flux will occur as the counter-ions in the double layer migrate to the oppositely charged electrode. The extent to which this increases the overall pore conductance is a function of the pore diameter to double layer thickness, i.e. $\frac{D}{\lambda_d}$. For $\frac{D}{\lambda_d} \gg 1$, a relatively thin double layer coats the inner pore surface and the effect of the surface charge extends only slightly into the pore. As a result, for the case of a thin EDL most of the solution contained within the pore is maintained at the bulk concentration and the conductance due to the surface charge can be neglected [51]. The reverse is also true. For $\frac{D}{\lambda_d} \geq 1$, the double layer extends deep into the pore structure and the bulk concentration assumption is no longer valid. It turns out that for the experimental conditions considered in this thesis the double layer thickness is on the order of 1 nm (calculated using equation 2.20

at room temperature and a 100 mM KCl solution) while the pore diameters were on the order of several hundred nanometers. Therefore for the remainder of the discussion the effect of the pore surface charge on pore *conductance* is neglected. However, it is an important consideration when designing pores with diameters on the order of 10 nm and should always be taken into consideration.

## 2.5 Theoretical signal

Nanopore sensing is based on the Coulter Counting technique [26] whereby the ionic current through a nanopore is reduced when a nanoparticle is present within it. The translocation of a nanoparticle causes a dip in the baseline current. The magnitude of the dip contains information on the particle size, the width of the dip is indicative of the translocation speed and the shape of the dip gives insight into the particle and pore's geometric properties. These signals will be assessed in the following subsections.

### 2.5.1 Current blockade – Particle sizing

The ionic current in a nanopore system is based on electrolyte transport from the cis to trans reservoirs through the pore. To this end, a current modulation is expected when an insulating nanoparticle partially obstructs the nanopore as it translocates through it. Over the past few decades several models of increasing complexity have been developed in an attempt to accurately predict the degree of current change during a translocation event. A representative few have been selected and presented here for illustration of the fundamental concepts and for their relevance in the experiment at hand.

#### *2.5.1.1 The Maxwellian Model*

The most simplistic view of current blockade due to a translocating particle takes advantage of Maxwell's model for the resistivity of a dilute suspension of insulating spheres in solution [52]. This model attributes the increase in pore resistivity to the displacement of ionic solution by the finite volume of the particle. Large particles will thus replace a larger fraction of electrolyte and a larger increase in resistance would be expected. Maxwell proposed that the effective resistivity of a dilute suspension of particles is related to the pure solution conductivity by:

$$\rho_{eff} = \frac{1}{\sigma_s}\left(1 + \frac{3f}{2} + O(f^2)\right) \tag{2.26}$$

where *f* is the solid fraction of the particles and $\sigma_s$ is the pure solvent (bulk) conductivity. For a single spherical particle inside a pore, the solid fraction is expressed as:

$$f = \frac{\forall_{sphere}}{\forall_{pore}} = \frac{2d^3}{3D^2L} \tag{2.27}$$

where d is the diameter of the particle, and D and L are the diameter and length of the pore, respectively. Equations 2.26 and 2.27 can be substituted into equation 2.18 for the pore conductance to yield the resistance of the pore when a particle is present:

$$R_2 = \frac{4L}{\sigma_s \pi D^2}\left(1 + \frac{d^3}{D^2L} + O(f^2)\right) \tag{2.28}$$

The change in resistance is then:

$$\Delta R = R_2 - R_1 = \frac{4L}{\sigma_s \pi D^2}\left(1 + \frac{d^3}{D^2L} + O(f^2)\right) - \frac{4L}{\sigma_s \pi D^2} = \frac{4d^3}{\sigma_s \pi D^4} \tag{2.29}$$

Notice that according to this model the change in resistance does not depend on the length of the channel. Furthermore there is a strong dependence on both the particle and pore dimensions. For a constant pore diameter, D, the theory predicts a sensitive dependence on increasing particle size. It is this physical concept that realized Coulter's original work of counting and sizing particulates in aqueous medium. Experimentally, equation 2.29 only holds for long channels and for particles much smaller than the diameter of the pore (d/D << 1), i.e. situations where the effects of curving field lines and charged structures are negligible. Although it is very limited in applicability, this volume exclusion model serves as a basic starting point for current modulation and provides a physically relevant analytical expression.

### *2.5.1.2 Integral resistance as a function of cross sectional area*

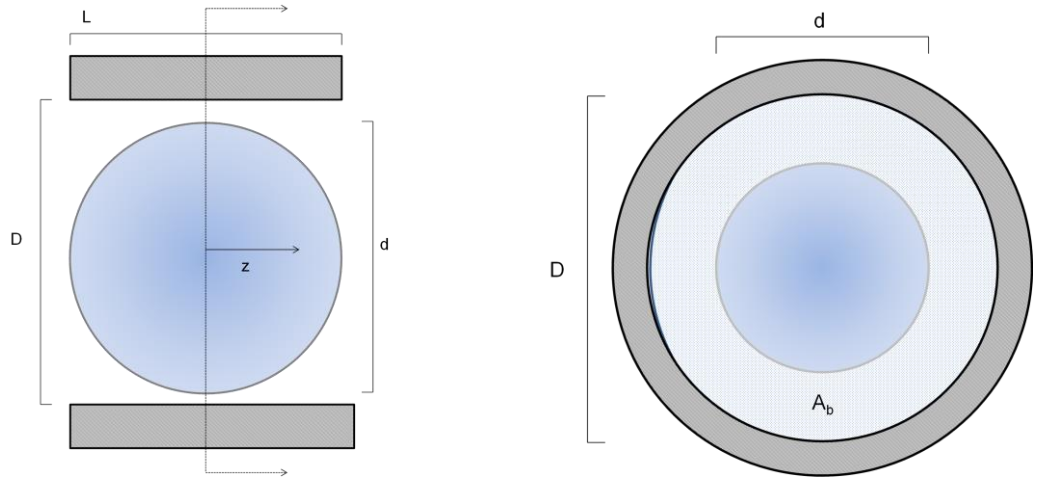


Figure 6: Particle with diameter, d, equal to the length of the pore, L. Geometry used in derivation of equation 2.31

One useful approximation to the resistance of a tube was presented by Deblois and Bean and later revisited by Bacri, et al. and is expressed as:

$$R = \rho \int_{-\frac{L}{2}}^{\frac{L}{2}} \frac{dz}{A(z)} \tag{2.30}$$

where L is the length of the pore and A(z) is a varying cross section as a function of distance into the pore. For a cylindrical unblocked pore, equation 2.30 gives an identical result to equation 2.13 for the pore conductivity. For a blocked pore, Bacri et. al. assumed a particle diameter equal to the total length of the pore and solved for the area between the particle and pore walls, $A_b$, as a function of z:

$$A_b(z) = \frac{\pi}{4}(D^2 - d^2) + \pi z^2 \tag{2.31}$$

Inserting equation 2.31 into equation 2.30 and performing the integration, the resistance of a blocked pore with the particle at its geometric center is:

$$R_b = \frac{4}{\sigma \pi D} \frac{1}{\sqrt{1-\left(\frac{d}{D}\right)^2}} atan\left[\frac{L}{D}\frac{1}{\sqrt{1-\left(\frac{d}{D}\right)^2}}\right] \tag{2.32}$$

The change in resistance is found by subtracting the blocked resistance from the open pore resistance:

$$\Delta R = R_o - R_b = \frac{4}{\sigma \pi D}\left[\frac{atan\left[\frac{L}{D}\frac{1}{\sqrt{1-\left(\frac{d}{D}\right)^2}}\right]}{\sqrt{1-\left(\frac{d}{D}\right)^2}}\right] \tag{2.33}$$

While this model gives reasonable results [31], it is not consistent across variations in pore diameters and lengths. This solution has proven accurate in cases where the particle diameter is on the order of the length of the pore and for thick pores (i.e. L/D >1), but does poorly in describing experiments where the pore length is shorter than its diameter and curving field lines have a significant effect on the current [14].

#### *2.5.1.3 The model of deBlois and Bean (Curving Electric Field Lines)*

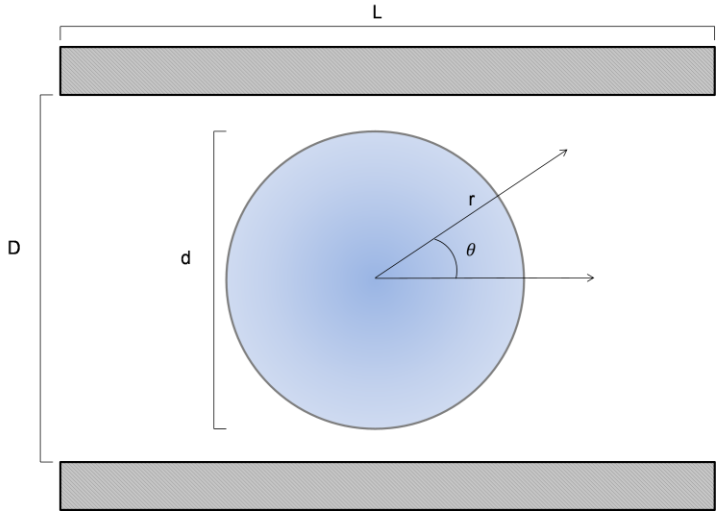


Figure 7: Definition of coordinate system used in equation 2.34.

The model of deBlois and Bean is developed from solutions to Laplace's equation for electric fields. Briefly, the derivation begins with a solution of Laplace's equation which accounts for insulating boundary conditions at the particle and pore surfaces given by (figure 7):

$$V(r,\theta) = \left(r + \frac{d^3}{16r^2}\right)\cos\theta \tag{2.34}$$

The current is then found by Ohm's law as:

$$I(z) = \frac{2\pi}{\rho}\int_0^{\frac{D}{2}} E_z x dx$$

$$E_z = -\frac{\partial V}{\partial r}\cos\theta + \frac{1}{r}\frac{\partial V}{\partial \theta}\sin\theta \tag{2.35}$$

The integration of equation 2.35 after including the expression for the electric field was shown by deBlois [54] to be:

$$I(z) = \left(-\frac{\pi D^2}{4\rho}\right)\left\{1 - \left[\frac{d^3}{(D^2+4z^2)^{\frac{3}{2}}}\right]\right\} \tag{2.36}$$

With the solution to the current at the center of the pore, $I(z = 0)$, and the potential difference found from the solution of Laplace's equation:

$$I(0) = \left(-\frac{\pi D^2}{4\rho}\right)\left\{1 - \left[\frac{d^3}{(D^2)^{\frac{3}{2}}}\right]\right\} \tag{2.37}$$

$$R_b = \frac{V\left(\frac{L}{2}\right) - V\left(-\frac{L}{2}\right)}{I(0)} = \frac{4\rho L}{\pi D^2}\left[1 + \frac{1}{2}\left(\frac{d}{L}\right)^3\right]\left[1 - \left(\frac{d}{D}\right)^3\right]^{-1} \tag{2.38}$$

While equation 2.38 solves exactly for the blocked resistance and applies to a larger range of experimental parameters, the solution has tended to be an overestimate [31, 41]. While deBlois & Bean suggested correction factors for specific cases of $\frac{d}{D}$, their analytical results were still applicable only for a finite range of pore and particle

geometries. This theoretical approach, however, did prove useful later in the development of more empirical and simulation based models.

#### *2.5.1.4 Semi-Empirical Model*

In recent years several semi-empirical models have been developed. Specifically, Davenport et. al., compiled experimental data, numerical results, and the above analytical solutions to develop an empirical model that is applicable over a wide range of pore and particle geometries. The experiment tested 50 nm and 100 nm particles in pores ranging in diameter from 200-300 nm and membrane thicknesses from 50-500 nm. Experimental current drops were recorded for several hundreds of translocation events and a histogram distribution was recorded as a function of percent current decrease from the baseline. From these histograms, Gaussian distribution curves were fitted and the peaks were taken to be the "most probable event depth" for a given set of parameters. To show a linear dependence of current drop on the volume exclusion principle, the authors plotted the experimentally determined most probable event depths as a function of the particle's volume fraction in the pore, $\frac{\Delta I}{I_o} = f(\chi)$:

$$\chi = \frac{2d^2}{3D^2} \; for \; d > L$$

$$\chi = \frac{2d^3}{3LD^2} \; for \; d < L \tag{2.39}$$

Note that this is already an improvement on the previous volume exclusion principle in that it takes into account particles smaller and larger than the thickness of the membrane. As one would expect, the current drop increased linearly for all cases. The authors

argued that if $\chi$ alone was an appropriate parameter, the slope of each curve would be nearly identical and very near to 1. However, this slope varied from 0.28 in the case of a thin membrane (L/D = 0.2) to 1.15 in the case of thick membranes (L/D = 1.5). Therefore the authors proposed a semi-empirical relation given by:

$$\beta = \begin{cases} 1, d \geq L \\ \frac{3}{2}, d \leq L \end{cases} \tag{2.40a}$$

$$\frac{\Delta I}{I} \approx \frac{\beta\chi}{1+\alpha} = \begin{cases} \frac{d^3}{\left(L+\frac{\pi D}{4}\right)D^2}, d < L \\ \frac{2d^3}{3\left(L+\frac{\pi D}{4}\right)D^2}, d = L \\ \frac{2Ld^2}{3\left(L+\frac{\pi D}{4}\right)D^2}, d > L \end{cases} \tag{2.40b}$$

where $\beta$ is a correction factor to account for the effect of curving field lines and was derived from the results of deBlois and Bean's solution, and $\alpha = \frac{R_{access}}{R_{pore}}$ is a correction factor for the contribution of the access resistance. It is also important to note that based on the findings of Tsutsui, et. al., it was assumed that the access resistance remains constant during particle translocations. Re-plotting the same experimental results against equation 2.40 as the abscissa, all of the curves approached a value of 1, confirming it as a more appropriate parameter in prediction of current drop magnitudes. In the limiting case of a small particle in a large pore, equation 2.40 approaches the simple solution presented by DeBlois & Bean and Bacri.

In summary, the above models were discussed in order of increasing complexity, accuracy, and breadth of application. In the end, a semi-empirical model was introduced and will be used in analyzing my experimental data. In brief, it takes into account volume exclusion, access resistance, the effect of curved field lines, experimental data, and various particle/pore geometries.

### 2.5.2 Translocation time – Particle and Pore Zeta-Potential

The second element in a nanopore signal is the duration of a translocation event. While the size of a particle is based on the degree of current drop, the zeta-potential of a particle can be derived from the time it takes to translocate a pore [28, 29, 31]. In general, the effective velocity of a charged particle is due to the sum of electrophoretic (EP), electroosmotic (EO), and pressure driven (PD) velocities [28]:

$$v_{eff} = v_{EP} + v_{EO} + v_{PD} \tag{2.41}$$

where EP and EO are the result of the interaction between a charged species and electric field and PD motion is due to an externally applied fluidic pressure. In the present study, no external pressure was applied such that the third term in equation 2.41 can be dropped.

Electrophoresis is defined as the motion of a charged particle through a solution when it is exposed to an electric field. In low Reynold's number flows, the drift velocity of a charged particle is directly proportional to the applied potential:

$$v_{EP} = \mu_e E \tag{2.42}$$

where $\mu_e$ is a constant of proportionality called the electrophoretic mobility. The electrophoretic mobility can then be related to the ζ-potential of the particle through the Smoluchowski equation [49]:

$$\mu_e = \frac{\varepsilon\zeta}{\eta} \tag{2.43}$$

where ε is the dielectric permittivity and η is the dynamic viscosity of the solution. The electrophoretic velocity is then:

$$v_{EP} = \frac{\varepsilon\zeta}{\eta} E \tag{2.44}$$

It is important to note that the Smoluchowski relation is valid only for relatively thin electric double layers, where the radius of the particle is much larger than the EDL. As calculated previously, electric double layers are usually at most one nanometer while the particles of interest are a hundred nanometers in diameter.

Electroosmosis is similar to electrophoresis except the frame of reference must be changed. In electrophoresis we assumed a charged particle moving under the influence of an electric field through a stationary medium. In electroosmosis, we instead fix the solid surface and study the motion of the charged ionic species (i.e. the fluid). As discussed previously, the electric double layer of a solid surface in contact with an ionic solution has an excess of counter-ions. Therefore there is a net charge very near to the surface. When a potential is applied, these counter-ions experience a net force toward the oppositely charged electrode and are set in motion. Due to shear stresses in the fluid, the counter-ions "drag" the fluid above it causing a net fluid flow. In general, the

electroosmotic velocity is found by simultaneous solutions of the Navier-Stokes and Poisson equations. After some simplification, the final differential equation is:

$$\varepsilon E \frac{d^2\varphi}{dy^2} = \eta \frac{d^2y}{dy^2} \tag{2.45}$$

Applying proper boundary conditions, the final velocity profile of the bulk solution far from the surface is:

$$v_{EO} = -\frac{\varepsilon\zeta}{\eta} E \tag{2.46}$$

The velocity profile is constant. In other words, in the case of a nanopore, electroosmosis is responsible for a plug flow type velocity profile within the nanopore caused by the motion of counterions in the EDL. The direction of flow is towards the electrode with same sign as the surface charge. For a negatively charged surface, the electroosmotic velocity is toward the negatively biased electrode. Therefore, for the case of a negatively charged particle and a negatively charged pore surface, the electrophoretic and electroosmotic velocities oppose each other and the effective velocity is:

$$v_{eff} = \frac{\varepsilon}{\eta}\left(\left|\zeta_{particle}\right| - \left|\zeta_{pore}\right|\right) \cdot E_{pore} \tag{2.47}$$

It is interesting to note that when the ζ-potential of the pore is greater than that of the particle, particles can translocate across the nanopore toward the like-charged electrode [18, 31].

With an experimentally determined translocation velocity and known $\zeta_{pore}$ , the $\zeta_{particle}$ of the particles can be determined. Equation 2.47 also suggests that it is possible to control the translocation velocity of a particle or DNA strand. This principle has been

the focus of several recent studies and pore surface charge modification and characteriation is a continuing area of research [18, 31, 33, 56, 57].

The translocation velocity in equation 2.44 is dependent on the potential drop across the pore. We have previously shown that the access resistance remains constant during a translocation event and therefore does not contribute to the detected signal [31, 54, 55]. However, we have also seen that in some cases the access resistance can be a major contribution to the total resistance of the pore system. This means that the access resistance serves only as a voltage divider whereby the potential drop across the pore is not equal to the applied potential at the electrodes. The true potential drop across the pore that should be used in equation 2.47 is:

$$\Delta V_{Pore} = \frac{R_{pore}}{R_{Pore}+R_{Acess}} \Delta V_{applied} \tag{2.48}$$

To be thorough, another resistance in the system is the potential drop across the EDL of the electrodes. Ag/AgCl electrodes were chosen in this experiment because they produce almost ideal Faradaic currents. The electrochemical reaction at the surface which produces free electrons in the electrode happens almost instantaneously at all applied potentials. This prevents charge buildup, capacitive effects, and renders the potential drop across its surface negligible. For a more detailed discussion of this additional series resistance, the reader is referred to The Axon Guide: A Guide to Electrophyisiology & Biophysics Laboratory Techniques [58].

# Chapter 3: Pore Fabrication and Experimental Considerations

## 3.1 Pore Fabrication and Conditioning

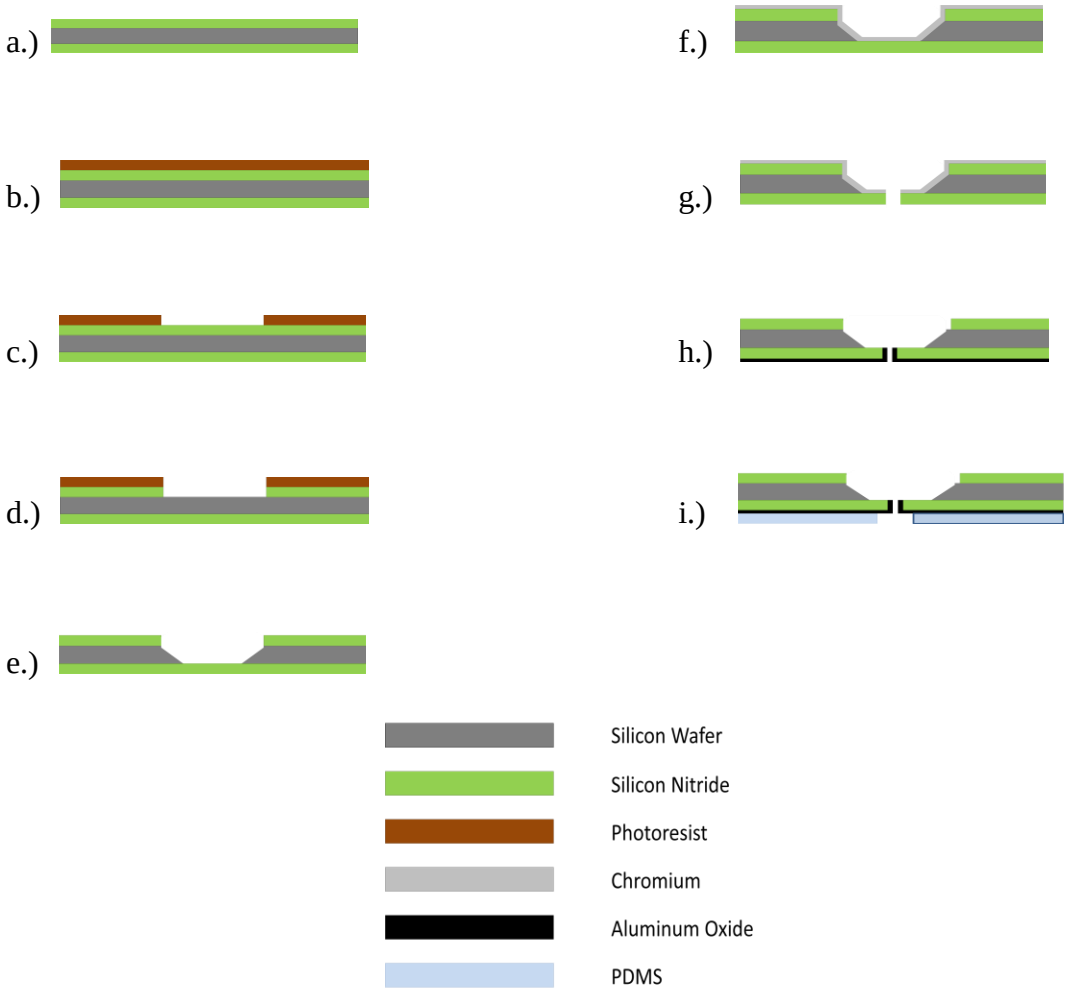


Figure 8: Fabrication Flow Chart: a.) 500 nm Silicon Nitride on 500 mm Silicon wafer b.) Spin coated photoresist c.) UV exposure followed by resist developer to remove exposed window d.) $CF_4$ RIE to remove silicon nitride (photoresist as etch mask) e.) Removal of remaining resist via NanoStrip. TMAH etch of silicon wafer (silicon nitride as etch mask) exposing a silicon nitride membrane on the backside f.) Evaporation of 30 nm of chromium g.) FIB milling of nanopore and simultaneous SEM measurement of pore diameter h.) Removal of chromium and ALD of 5-20 nm of aluminum oxide depending on desired final pore diameter i.) Application of a PDMS layer via single loop brush and micromanipulator. Piranha cleaning was performed before step a.), after step f.) and again after step h.) before application of the PDMS layer. Both sides of the chip in step i.) were exposed to a low power oxygen plasma to enhance hydrophilicity immediately before testing.

Pores were fabricated in 500 nm thick, low-stress silicon nitride membranes supported by 500 um thick silcon wafers. Whole wafers were first cleaned in boiling Piranha (1:2, 30% Hydrogen Peroxide:Sulfuric Acid) solution for 10 minutes followed by drying on a hotplate. To enhance photoresist adhesion, a coat of HMDS was applied to the wafer. AZ5209E photoresist was spin coated onto the surface at 2000 rpm for 60s. Following a 90 second soft-bake, the wafers were exposed to UV light for 12 seconds under a positive photomask. AZ726MIF developer was used to remove the exposed sections of resist leaving an array of square silicon nitride windows on one side of the wafer surface. The remaining photoresist was used as an etch mask during a $CF_4$ reactive ion etch (RIE) step, which removed the exposed silicon nitride leaving behind an array of bare silicon squares. The remaining photoresist was removed using room temperature NanoStrip before the entire wafer was submerged in a TMAH (4% by mass) solution for 12 hours. Due to the highly anisotropic etching of the < 111 > and < 100 > planes, pyramidal pits were formed with small (~100x100μm) suspended nitride membranes left at the bottom surface. To prevent charge buildup in the SEM, 30 nm of chromium were evaporation deposited on the window side of the wafer. Nanopores were drilled through the chromium and nitride layers using the focused ion beam (FIB) in a FEI Strata Dual Beam system. Depending on the Ga+ ion dosage, pore sizes ranging from 300 nm to 1 um in diameter could be accurately milled. The pores were then measured using the SEM of the same system and the chromium layer was subsequently removed. Individual

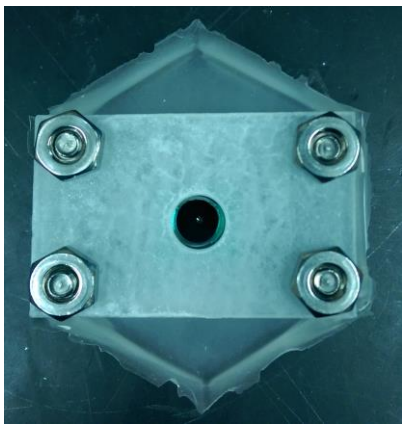

Figure 9: Flow cell assembly. A nanopore chip is compressed between two PDMS gaskets. Acrylic is used as a mechanical support for the securing screws.

chips were then separated by cleaving and cleaned for 4 hours in Piranha. This also improved the hydrophilicity of the pores. Atomic layer deposited aluminum oxide was then used for several reasons. First, $Al_2O_3$ has a lower surface charge density than silicon nitride which facilitates particle translocation via a reduced $\zeta_{pore}$ in equation 2.47 [59]. In addition, the atomic layer precision coupled with high conformity of the ALD process allows for further reduction of pore size if required. Finally, an additional dielectric layer was added to assist in noise reduction, which will be discussed in further detail when noise issues are addressed [59]. A thin (~100 um) layer of PDMS was spread onto the chip surface and cured at 75˚C for 2 hours to further assist in capacitive noise reduction. A low-power 10 second oxygen plasma exposure was necessary in hydrophilicizing the nitride and PDMS layers after long storage periods in air. Chips were placed in a custom flow cell made from PDMS and acrylic. The final assembly is shown in figure 9.

## 3.2 Experimental Setup

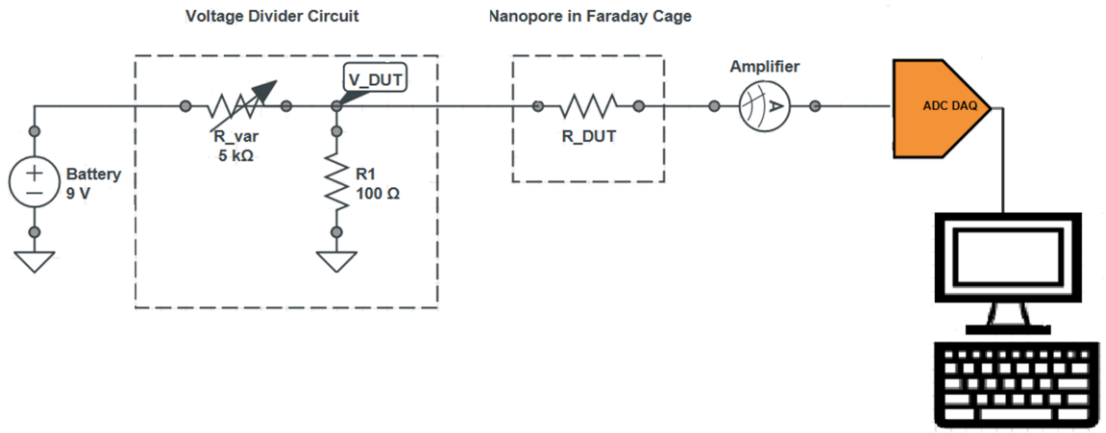


Figure 10: Schematic of Experimental Setup

Figure 10 shows a schematic of the experimental setup. A 9V battery was used as the driving potential to reduce the main line 60 Hz noise (see "Noise Sources and Noise Reduction"). Because only 100-300 mV were required, the battery was connected to a voltage divider circuit consisting of a variable resistor ($R_{var}$) connected in series with a 100 Ω resistor ($R_1$), which is eventually in parallel with the pore ($R_{DUT}$). Since the total resistance of resistors in parallel is dominated by the smaller value, the voltage drop across the pore (~5 MΩ) will be constant even during particle translocation. The output voltage from the divider circuit as a function of $R_{var}$ is given as:

$$V_{out} = \frac{\frac{R_1 R_{DUT}}{R_1 + R_{DUT}}}{\frac{R_1 R_{DUT}}{R_1 + R_{DUT}} + R_{var}} \cdot V_{Battery} \tag{3.1}$$

and is shown in figure 11.

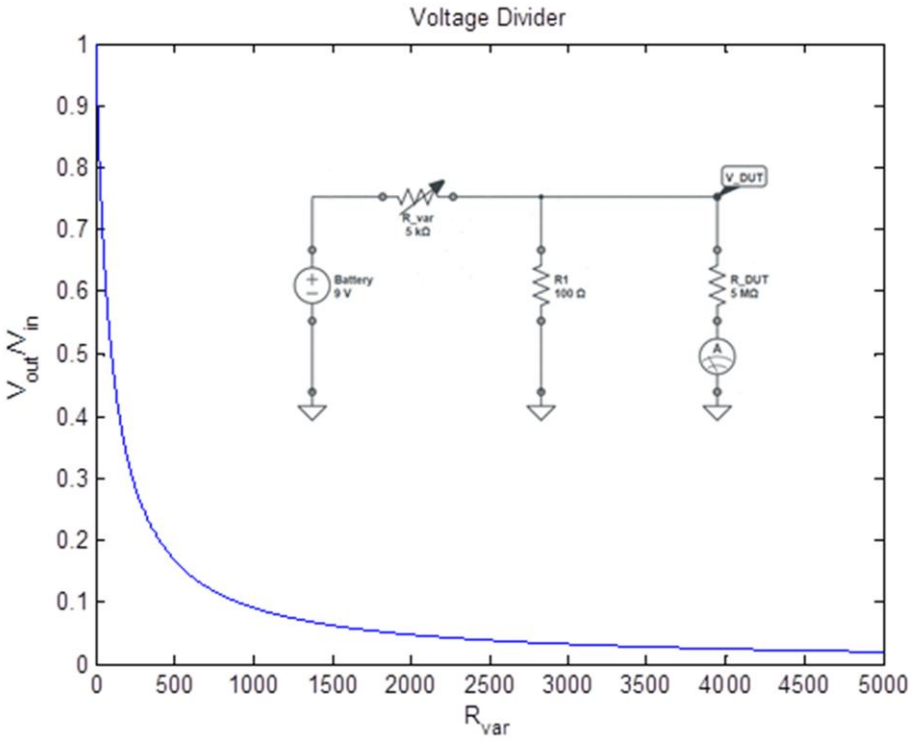


Figure 11: Voltage divider circuit and V_DUT as a function of $R_{var}$

The output voltage of the divider circuit is dropped across the nanopore via Ag/AgCl electrodes within a grounded Farday Cage (see "Noise Sources and Noise Reduction"). The entire system is grounded together via the BNC connector outer casings. The resulting current is amplified by a Model 1211 Current Amplifier (DL Instruments, LLC) and is output as a proportional voltage. The voltage is then sampled by a National Instruments data acquisition board at 100 kHz and monitored and recorded in LabView. Shielded cables were used in all electrical connections between systems.

### 3.3 Equipment Specifications, Bandwidth, and Discrete Time Sampling

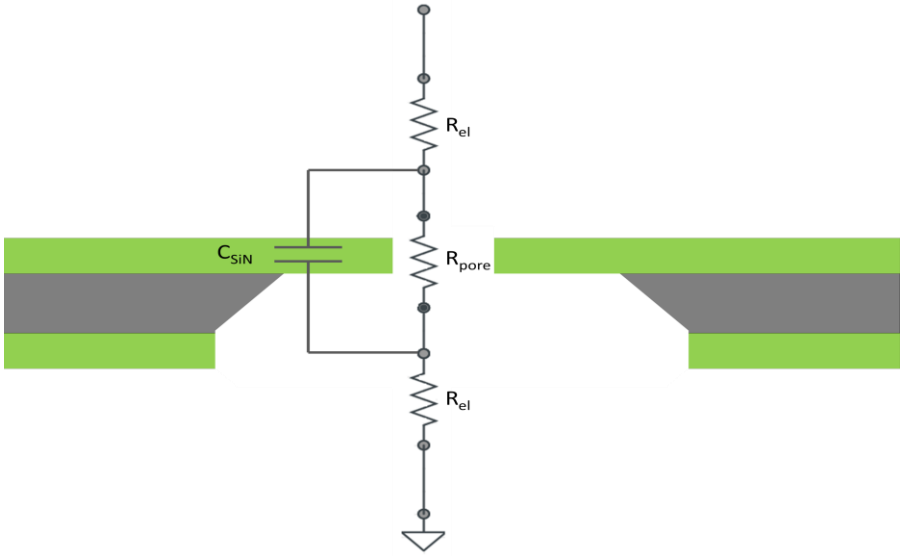


Figure 12: Simplified equivalent circuit diagram of nanopore device.

In all nanopore based sensing experiments there is an eternal struggle between speed and noise. Typical current drops during translocation are on the order of tens of nanoamperes and event durations can range from a few microseconds to a millisecond [28, 31, 54, 55, 57, 60]. Unfortunately, noise and speed are directly related in most electronic components. System considerations pertaining to speed will be discussed in this section and noise reduction will be addressed later in the report.

One of the most important specifications of an analog amplifier (i.e. for *continuous* signals) is its bandwidth, which is defined as the range of frequencies that can be faithfully followed. The 10-90% rise time of a system is a more intuitive parameter, but less cited in equipment specifications. The two are related simply by [61]:

$$f_c \cong \frac{0.35}{t_{10-90}} \tag{3.2}$$

The bandwidth of the amplifier decreases with increasing sensitivity. For example, 100 nA/V, 10 nA/V and 1 nA/V outputs have specified bandwidths of 25 kHz, 13 Khz, and 4 kHz, respectively. Using equation 3.2, these correspond to 10-90% rise times of 14 µs, 26 µs, and 85 µs, respectively. Since our particular signal is expected to be on the order of 0.1-1 nA and a few hundred microseconds in duration, the 10 nA/V setting was chosen.

In all analog systems there is an inherent bandwidth, i.e. the inverse of response time, of the device under test. To a first approximation, the nanopore can be modeled as an equivalent circuit of resistors and capacitors. A schematic is shown in figure 12. The cutoff frequency, $f_{cp}$, of the pore arises from the simple RC circuit of the electrolyte resistance in series with the membrane capacitance [61]:

$$f_{cp} \approx \frac{1}{2\pi R_{el} C_{SiN}} \tag{3.3}$$

More complex equivalent circuit models have been derived for pores which include parallel capacitances and resistances of the silicon wafer, various depletion layers and electric double layers at solid/solution interfaces. The reader is encouraged to read the works of Dimitrov [63] and Smeets [62] for a more in depth discussion. However, in the context of speed, these equivalent circuits still predict a pore bandwidth on the order of MHz. The device bandwidth is therefore not a limiting factor in the speed of measurements.

The voltage leaving the amplifier must be sampled and stored via the data acquisition board. The sampling frequency in digital, discrete time systems is an analogous parameter to the bandwidth in continuous, analog systems. Just as in the analog case, the fidelity of the digitally reproduced signal is directly related to how quickly the real signal is recorded. In an extreme example, a 1 kHz sampling frequency samples the signal once every 1 ms. Therefore a particle translocation event lasting 500 μs would not be detected. Another error that can occur during signal processing is called aliasing whereby a real signal of high frequency cannot be accurately represented by the digitized data and is instead mistaken as a signal of much lower frequency. To prevent aliasing, a general rule of thumb is to sample at twice the speed of the fastest expected signal. This is referred to as the Nyquist frequency and sets the lower limit. For the current experiment, a 100 kHz sampling frequency (10 μs between points) was determined to be appropriate for accurately depicting the expected signal.

## 3.4 Noise Sources and Noise Reduction

While large bandwidths are required for recording fast translocation events, they are inherently associated with noisier signals. The following section gives an overview of the various sources of noise in the low and high frequency regimes, how they can be eliminated, and experimental results.

### 3.4.1 Stray Electromagnetic and Physical Noise Sources

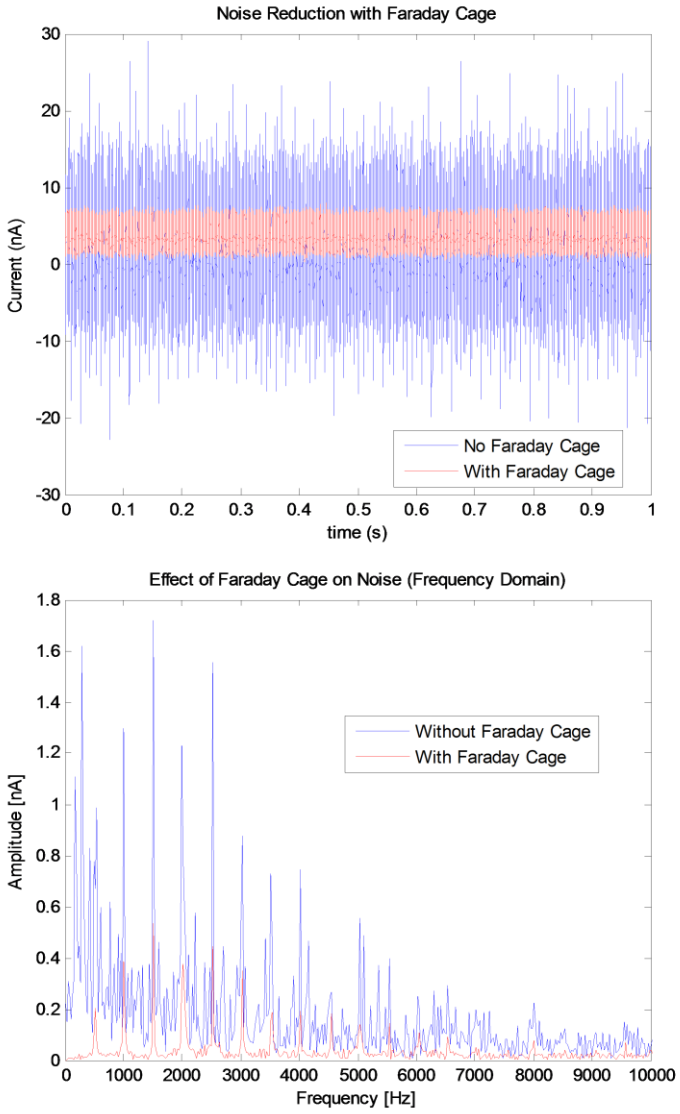


Figure 13: Noise reduction with the inclusion of a Faraday Cage.

Stray electromagnetic pickup comes from a variety of sources ranging from noisy computer screens to ubiquitous RF waves in the air [58]. To mitigate these noise sources, it is common practice to use short, shielded cables between all electrical components. In

addition, it is often necessary to shield the pore, electrodes, and sensing equipment inside a Faraday cage, which is a continuously conducting enclosure which blocks EM radiation. Faraday showed that when exposed to an external electric field, electrons on the skin of the conducting metal cage rearrange and cancel the incoming field. As a result, the interior is unaffected. In a practical example, a microwave is an effective Faraday cage preventing the EM waves generated within it from escaping. The concept is identical in low level electrochemical measurements and Faraday cages have become essential components in such experiments [12, 29, 33, 57, 60, 65, 66]. Figure 13 shows a significant reduction in noise when a nanopore and accompanying electrodes are housed in a cage versus open to a noisy lab environment.

Another example of stray electromagnetc noise is that from the main-line power source also known as “hum”. In early experiments, the driving potential was supplied by the data acquisition output connection and was highly contaminated with main line noise. In the frequency domain, this presented itself as large amplitudes centered at 60 Hz and in the time domain large current spikes were observed at regularly spaced intervals every 17 ms. Figure 14 shows the time domain of noise introduced by the main line. The hum was eliminated by replacing the power source with an external 9V battery whose potential was modulated by an adjustable voltage divider circuit (see figure 11).

Large baseline fluctuations were observed in several pores and were attributed to incomplete wetting. Similar results have been seen in the works of Beamish et. al. To ensure total wetting, the pores were treated with either a low-power oxygen plasma or

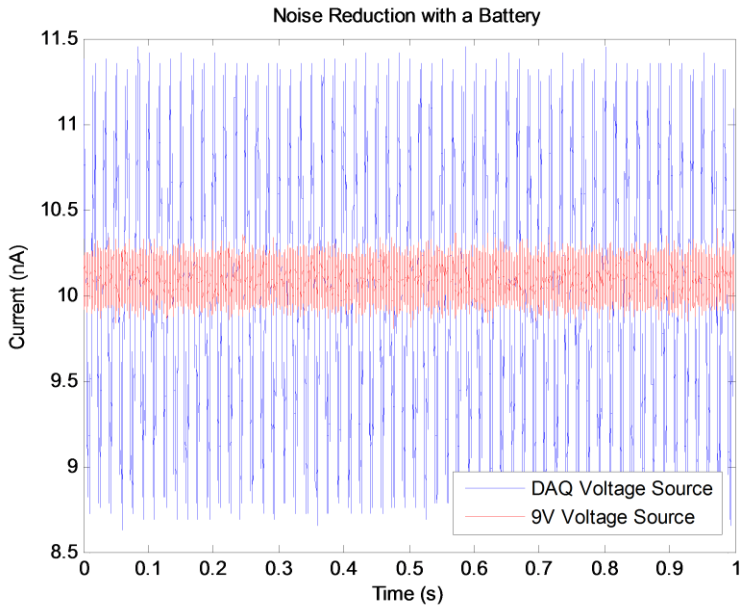


Figure 14: Noise reduction by replacing the DAQ voltage source with a 9V battery voltage source. Notice the discrete peaks from the 60 Hz main line "hum" present in the DAQ source.

exposed to a Piranha cleaning step [67]. Furthermore, the technique of Beamish was periodically used where short bursts of high electric potential asymptotically increased the baseline current [67].

Despite the entire setup situated on top of a passive optical table, heavy footsteps, slamming doors, and other large physical perturbations were also present in some signals. In many cases, the signal resembled an underdamped spring resulting from induced vibrations in the cantilever electrodes. In most cases the electrolyte eventually dampened the perturbation and the experiment was able to continue within a few seconds.

### 3.4.2 Low-Frequency Sources

Thermal noise usually sets the lower limit in nanopore based systems and is generated by thermal fluctuations in conducting media [41]. Also known as Johnson noise, the root mean square (RMS) can be expressed as:

$$I_{thermal_{RMS}} = \sqrt{\frac{4kTB}{R}} \tag{3.4}$$

where k is the Boltzmann's constant, T is the temperature in K, B is the bandwidth and R is the resistance [61]. In many cases, the $I_{RMS}$ is on the order of a few pA and can therefore be reasonably ignored.

By far the largest low-frequency noise is the so-called flicker noise. Otherwise known as 1/f noise owing to its inversely related proportionality to frequency, its origins have not been completely understood [41, 59, 61, 63, 65]. In general, the source of the noise is commonly attributed to conductance variations in the pore [68], but this is usually where agreement between researchers begins to diverge. For example, Smeets et. al. [62], proposed that pore surface charge fluctuations are the major contributor, while Hooge [69] argued that the variability in charge mobility is to blame. Charge fluctuations on the pore wall were addressed with the atomic layer deposition of aluminum oxide, but no further attention was paid in explicitly reducing 1/f noise any further. Fortunately, high-frequency noise sources were better understood and more readily reduced.

### 3.4.3 High-Frequency Sources

Two noise sources prevalent in the high frequency domain (up to 10 kHz) are the dielectric noise of the pore structure and the input capacitance noise of the coupled pore/measurement system combination [41, 58, 61].

All real dielectric materials display some losses, which in turn generate thermal noise. The RMS dielectric noise has been shown to be dependent on the capacitance of the membrane and support chip, $C_{chip}$, and dissipation factor, D, of the material as:

$$I_{Dielectric_{RMS}} = \sqrt{4kTDC_{chip}\pi B^2} \tag{3.5}$$

where B is the bandwidth of the system [41]. The capacitance of the chip is a combination of several factors, including the membrane and silicon support chip, the EDL on surfaces exposed to the electrolyte, and the depletion layer between the silicon and its native oxide [63].

A second capacitance-dependent high-frequency noise source is the input capacitance noise and is a dominating source at frequencies greater than 10 kHz. Resulting from the combination of voltage noise at the amplifier input and the sum of the capacitances of the system, the RMS input capacitive noise is described by:

$$I_{input_{RMS}} = \sqrt{\frac{1}{3}f^3(2\pi C_{total})^2 e_n^2} \tag{3.6}$$

where $e_n$ is the equivalent voltage noise at the amplifier input and $C_{total}$ is the capacitance of the entire system [41]. Equations 3.5 and 3.6 show a clear dependence on both the

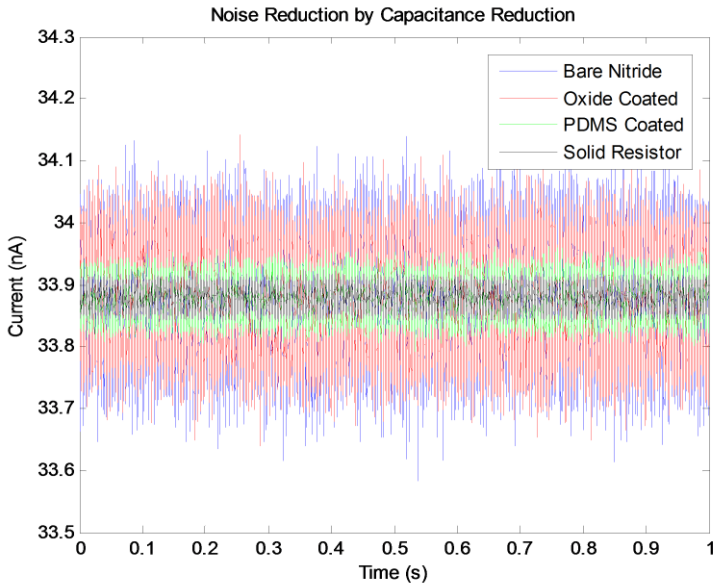


Figure 15: Capacitive noise reduction by addition of PDMS and Aluminum Oxide. Noise in solid resistor is added for comparison to minimal capacitive element.

bandwidth of the system as well as the capacitance of the chip. While the amplifier has built-in analog filters, the high bandwidth required for nanoparticle detection restricted their use. As a result, the focus was shifted toward reducing the chip capacitance by coating the pore with various dielectric layers.

As previously mentioned, ALD aluminum oxide was explored as an option to reduce chip capacitance. Because atomic layer deposition is a conformal process, any deposited oxide inherently reduced the size of the pore. While this is a desired effect for fine tuning the diameter of the pore to better match the size of the particles, it also sets the upper limit of the thickness that can be deposited. As a result, the oxide layer was too thin to reduce the capacitance of the chip by any appreciable amount (see figure 15). The

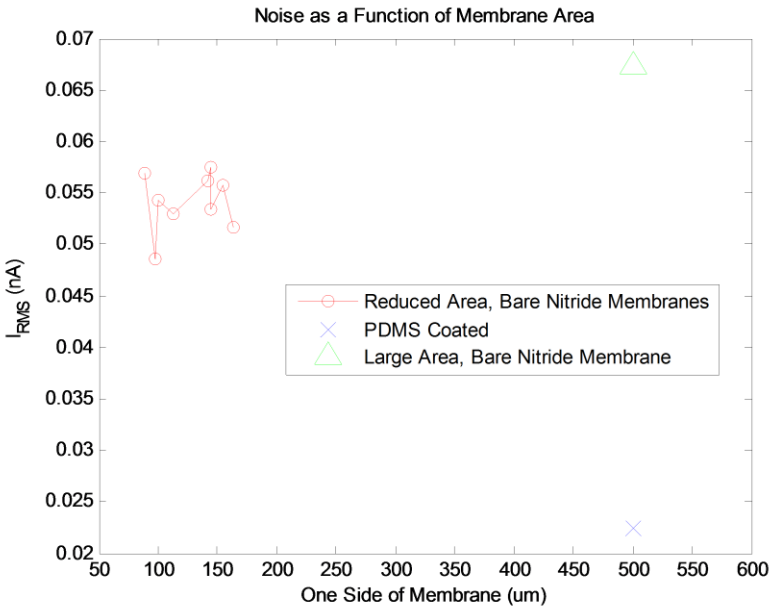


Figure 16: Noise as a function of reduced membrane area.

capacitance of a dielectric is directly proportional to its area. As a result, a study of reducing the suspended silicon nitride membrane area was conducted. Membrane areas up to 5 times smaller were fabricated and tested, but were also unable to provide significant noise reductions over their larger counterparts (see figure 16). While reducing the membrane size reduced the capacitance of the suspended nitride, it does not have any effect on eliminating the capacitance of the rest of the exposed, non-suspended, silicon nitride in contact with the solution. To assuage this problem, a similar approach to Tabard-Cossa, et. al., was adopted whereby a thick (~100s of µm) layer of PDMS was applied everywhere on the chip surface [65, 70]. PDMS (10:1) was first applied in small drops on the surface of the device. Using a micromanipulator and a custom single-loop brush, the droplets were spread onto the entire surface of the chip, leaving only a

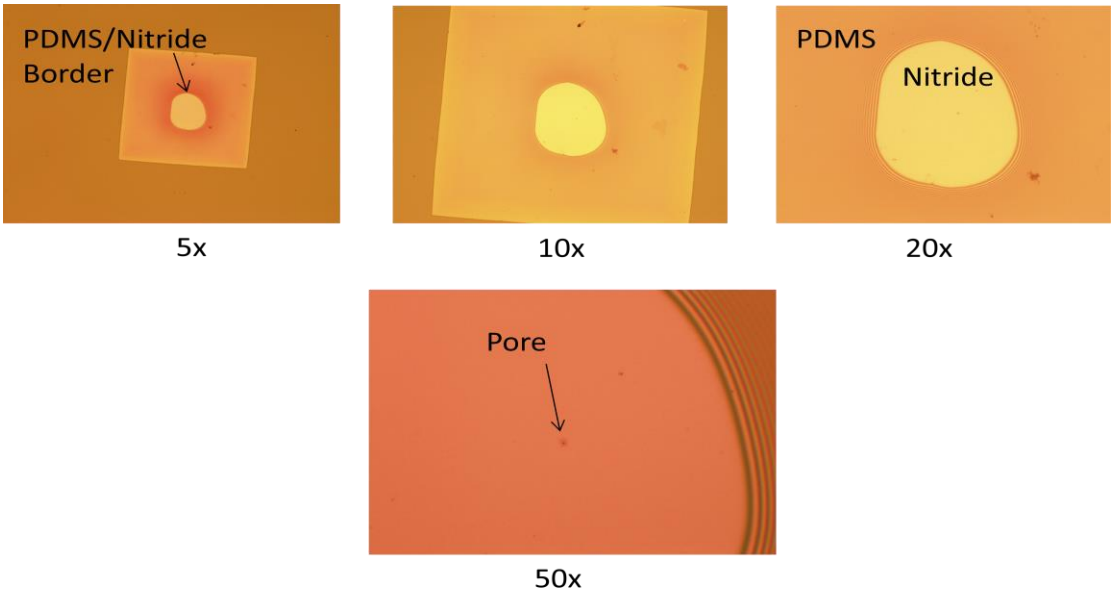


Figure 17: Optical micrograph of PDMS painted onto Silicon Nitride

100x100 um area of exposed nitride around the pore. The PDMS was cured at 75˚C for 2 hours. An optical micrograph of the final structure is shown in figure 17. A significant reduction of RMS noise was observed (figure 15) and is compared to that in a solid resistor, which was presumed to set a lower limit on the capacitive noise. Because PDMS is inherently hydrophobic, the chips were exposed to a low-power oxygen plasma immediately before tests. While particle translocation events were detectable, PDMS is difficult to clean by standard procedures and, as a result, each pore was rendered a single-use only device.

In summary, noise reduction occurred in several steps each increasing in sensitivity. Large (~10 nA) reductions were initially made from the blocking of stray electromagnetic radiation by enclosing the pore and electrode structure within a dark Faraday Cage. Next, main line “hum” noise was eliminated (~5 nA reduction) by

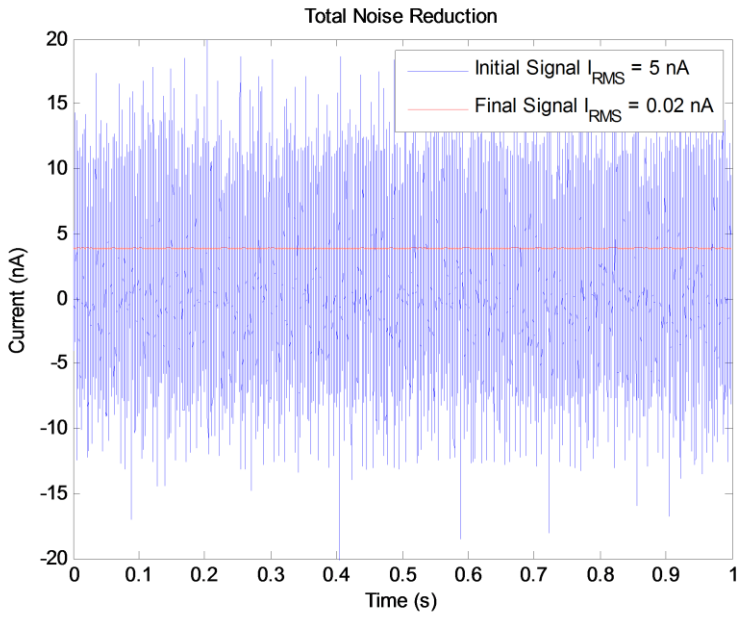


Figure 18: Total noise reduction after inclusion of: Dark Faraday Cage, 9V battery voltage source, complete wetting, reduced membrane area, and aluminum oxide and PDMS layers.

replacing the digital to analog output of the DAQ with a quiet, 9V battery as the driving potential. The focus was then shifted from the electronics to the chip itself, and oxygen plasma and Piranha solution were used to increase the hydrophilicity of the pore (~1 nA). Finally, the high frequency capacitive noise was reduced by coating an entire surface of the device with a thick, PDMS layer (~0.5 nA reduction). The RMS noise was reduced by 3 orders of magnitude from 10 nA to a final value of approximately 0.02 nA and is shown in figure 18.

## 3.5 Nanoparticle Preparation and Characterization

Polystyrene nanoparticles were manufactured by and purchased from Invitrogen Molecular Probes. All experimental results were conducted with 100 nm, carboxylate-

modified polystyrene spheres at a final concentration of $10^{11}\ \frac{particles}{mL}$. Anhydrous potassium chloride was purchased from Sigma Aldrich and prepared in 18 MΩ·cm deionized water at various molar concentrations. The electrolyte solution was filtered through 200 nm TEFLON PTFE Membrane Syringe Filters manufactured by Nalge Nunc International before the nanoparticles were introduced. The particles and stock KCl solutions were stored separately in a dark, cool environment until just prior to each experiment. To ensure a monodisperse population of particles, 1 mL aliquots of nanoparticle suspensions in KCl were sonicated for 5 minutes immediately before introducing it to the flow cell.

Nanopore sensing is a complex interplay between not only the particle and pore, but also with the suspending solution and electronic specifications. Each of the experimental parameters is intricately paired with all the others and changes to one can have profound effects on the results. The next few subsections will delineate the key relationships between them and the important considerations that were made in selecting the proper conditions for the following experiments. Because it is easy to get lost in the interplay between parameters, the effect of the KCl concentration will serve as the backbone parameter by which all others will be affected.

### 3.5.1 Considerations in KCl Concentration – Optimizing Ionic Current and Noise

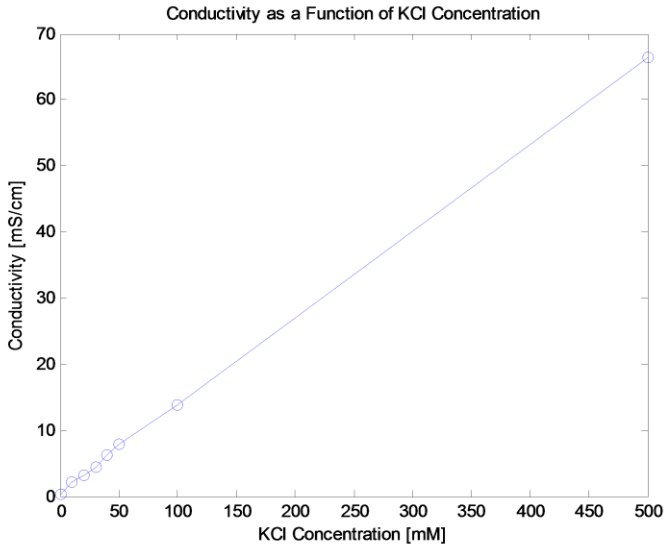


Figure 19: Electrolyte conductivity as a function of KCl concentration.

The resistance of a pore is inversely proportional to the conductivity of the solution, which in turn is directly proportional to the concentration of the electrolyte (figure 19). As a result, with the electric potential bias ranging initially from 100 to 500 mV (the bias was later experimentally adjusted to produce a valid signal), the electrolyte concentration must be selected such that the resulting current through the pore does not overload the amplifier at a given sensitivity. In turn, the sensitivity of the amplifier largely affects its noise and bandwidth capabilities. As discussed previously, the 10 nA/V setting was selected based on the theoretical signal magnitudes (equation 2.40) of 100 nm particles in 300 – 500 nm pores. With this sensitivity and the ±10V dynamic range of the amplifier, the maximum current through the pore was limited to ±100 nA.

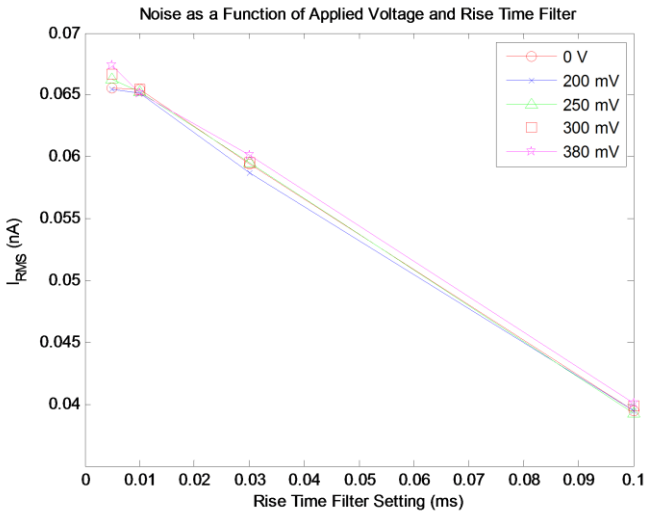


Figure 20: Noise as a function of applied voltage and amplifier rise-time filter.

Given the range of experimental pore diameters, potential biases, and equation 2.17, KCl concentrations between 0 and 200 mM could be used without overloading the amplifier (figure 19). According to equations 2.40, a larger baseline current results in a larger absolute increase in the signal when a particle travels across the pore. As shown in figure 20, the noise does not depend on the voltage applied. Therefore, without any further considerations, it is logical to assume that a large as possible baseline current is desired such that the SNR is maximized. This would lead one to select a large as possible KCl concentration before overloading the system. However, there are other restrictive dependencies limiting the KCl concentration that are addressed next.

### 3.5.2 Considerations in KCl Concentration – Nanoparticle Stability and Translocation Velocity

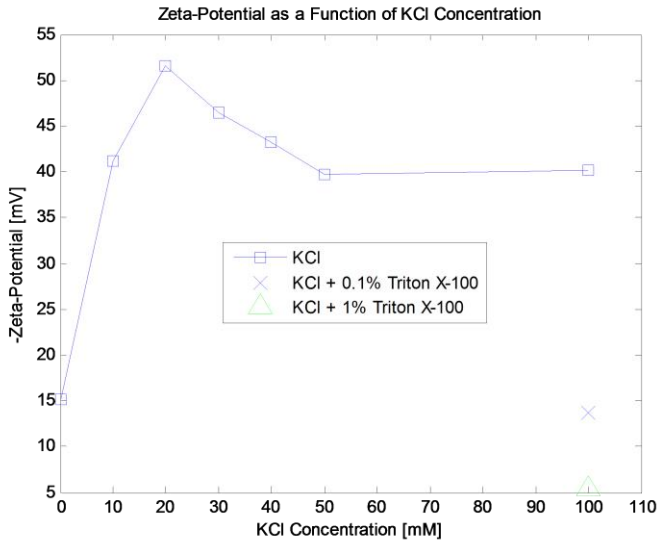


Figure 21: ζ-Potential as a function of KCl concentration

In addition to its effect on the electronic components of the system, the electrolyte concentration also plays a vital role in determining the ζ-potential of the nanoparticles in solution. Consequently, the ζ-potential controls both the particles' stability as well as translocation velocity.

As was discussed in the "Surface Charge, Zeta-Potential, EDL, and Debye Length" section, the concentration of the electrolyte solution is a main contributor to the ζ-potential of a charged surface. As a brief summary, the ζ-potential is defined as the electric potential at the slipping plane of the EDL after electrolyte shielding. Equations 2.20 and 2.25 for the electric double layer thickness and electric potential as a function of distance from the surface, respectively, show that for increasing concentrations of KCl

the ζ-potential decreases. In other words, the charge of a surface is more effectively shielded when more counter-ions are present in the solution. In the context of nanoparticles, stability in solution is defined as the ability of the particles to resist agglomeration and to exist as a monodisperse population. The stability of nanoparticles is directly related to their ζ-potential, as larger magnitude like-charges more effectively repel each other [48, 71]. The larger the potential, the more likely the surfaces are to overcome attractive Van der Waals forces and remain as individual particles [48, 71]. It is generally accepted that nanoparticles with ζ-potentials greater than ±30 mV are stable [16, 17, 30, 48]. The carboxylate molecules adsorbed onto the polystyrene nanoparticle surfaces give rise to a negative surface charge. The variation of ζ-potential as a function of KCl concentration was determined by DLS and is shown in figure 21. The non-monotonically decreasing potential with increasing concentration is not uncommon [16, 17, 30]. While the exact origin is not completely agreed upon, one explanation is that there is a concentration at which the adsorption of negative Cl- ions in the interfacial region at the hydrophobic surface of the particle is at a maximum [16]. From figure 21, it appears that the nanoparticle suspension will be stable for the given range of KCl concentrations from the previous section. However, this was a fortuitous result and the reader is encouraged to conduct this study for every new particle population received. Depending whether or not the surface is functionalized (and which functional groups exist if it is), the ζ-potential can vary by more than an order of magnitude and particles can be extremely susceptible to agglomeration. Besides determining stability, the ζ-

potential of a particle affects its translocation velocity according to equation 2.47. For high salt concentrations, the ζ-potential will generally decrease, requiring large driving potentials which have the added risk of overloading the amplifier. In contrast, at low salt concentrations, even moderate potential biases could cause translocation speeds much faster than the rise-time of the amplifier. In addition, the low potential biases would generate low baseline currents, which would decrease the SNR according to equations 2.40 and figure 20.

To summarize, the concentration of electrolyte must be carefully considered as it not only affects the selection of the sensitivity of the preamp (which in turn affects its speed), but also the stability of the nanoparticles in suspension through its effect on their ζ-potential. In addition to stability, the ζ-potential also determines the speed at which the particles travel through the pore for a given potential bias. The bias, in conjunction once again with the electrolyte concentration, controls the baseline current level and therefore the SNR. At the same time, however, the bias must be maintained at a small enough magnitude such that the speed of the particles does not approach the limited rise-time of the amplifier and the baseline current does not overload the amplifier. A 100 mM KCl concentration meets all of these requirements and was used in all of the following experiments.

# Chapter 4: Results and Discussion

## 4.1 Pore Resistance – IV Curves and In-Situ Diameter Measurements

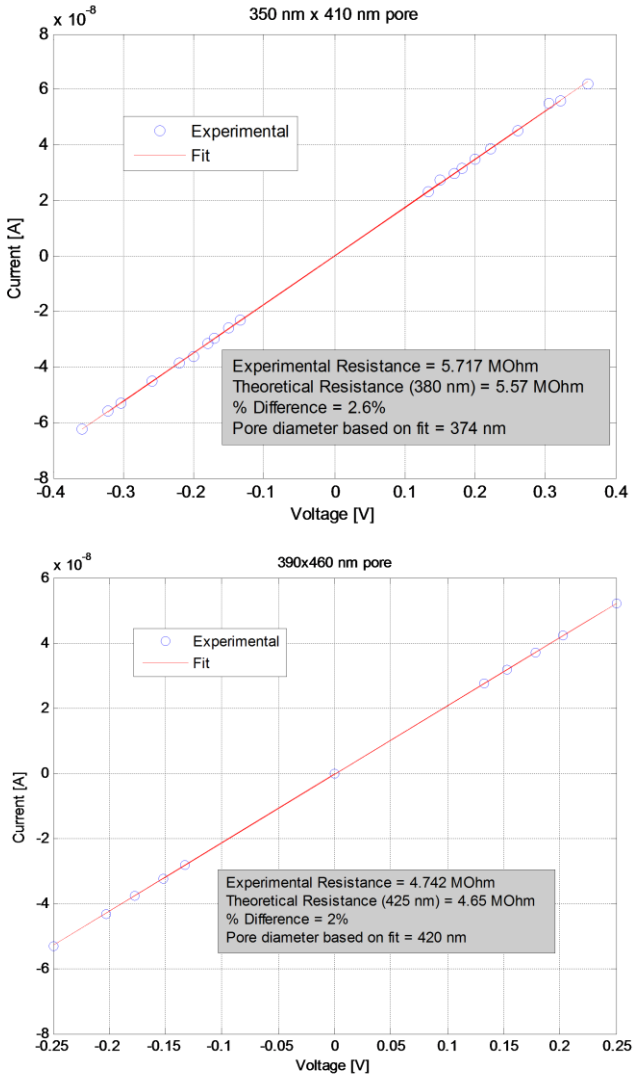


Figure 22: Representative IV curves of two pores used in the experiments.

I-V curves of every pore in solution were constructed. Experimental resistances were derived from the inverse slope of the curves and compared to the theoretical value

predicted by equation 2.17 and the SEM determined diameters. Since the ion beam of the FIB was subject to a slight drift during the drilling process (the degree of drift is dependent on the accuracy of the focus and stigmation of the beam), many of the pores were elliptical in cross section. In the event of a non-circular pore, a geometric diameter (average between major and minor axis diameters) was used in equation 2.17 [51]. Figures 22 show representative curves of two independent pores. Because of the nature of the voltage dividing circuit used to adjust the potential across the pore, there exists a lower limit of voltage that can be applied. Potentials less than approximately 0.13V could not be attained. However, the points tested in the I-V curves are the range of potentials used in the actual experiments and are therefore a good representation of the resistance properties of the pores in their testing environment. The geometric diameters used in determining the theoretical pore resistance are shown in the inset of the plots. A pore diameter based on the experimental resistance and equation 2.17 is also shown in the inset. Experimental voltages were selected at random to prevent any effects of hysteresis.

All I-V curves showed a linear dependence of current on voltage. This suggests a uniform cross-section through the length of the pore. This justifies the assumptions made in the derivations of equations 2.30-33. Ion-current rectification has been shown to be the result of varying cross-sections in pores in several experimental results [33, 59, 71-73]. The pores used in the works of Chen, Yusko, Kraynov and Kovarik had very large cone angles, which were the result of the higher inaccuracies related to small pores (~1 nm), or intentional widening of the pore entrance relative to its exit. While FIB drilling

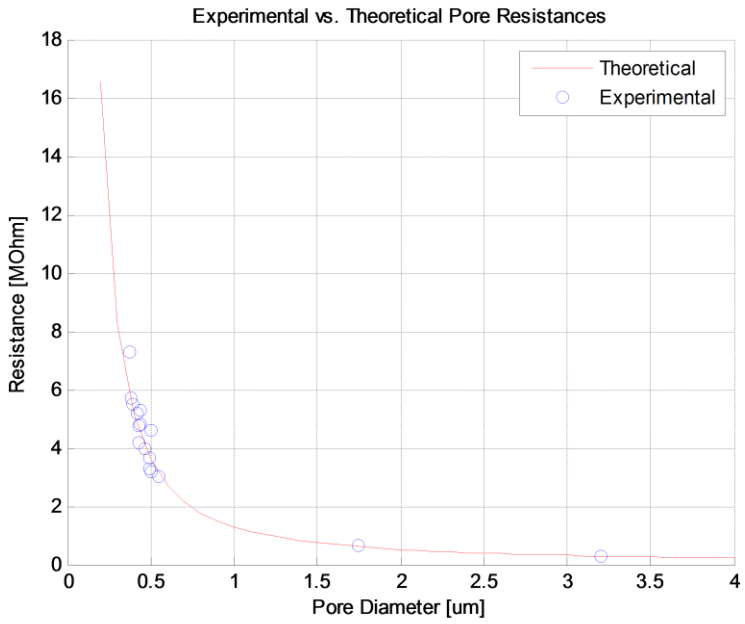


Figure 23: Experimental pore resistances as a function of diameter. The red curve represents the theoretical pore resistance based on a 500 nm thick pore.

has shown to produce slightly varying cross-sectional pores, the relatively large diameters (300 - 500 nm) reduced this effect [57].

The assumption of bulk conductivity within the pore in equation 2.17 is also validated due to the relatively large diameter of the pores, and can be justified by the small degree of error between the theoretical and experimentally determined resistances. Figure 23 shows a plot of the experimentally determined pore resistances (blue open circles) superimposed on their theoretical resistances based on an assumed 500 nm length. The experimental data clearly reflects the high sensitivity of the resistance on pore diameter within the range tested. This high sensitivity allowed for precise in-situ measurements of pore diameters and provided for a quick quantitative validation before the introduction of particles. It was found that pores with less than 15% difference

between their experimental and theoretical resistance values were more likely to allow for particle translocations. Above this error, immediate and irreversible clogging was observed. Resistances much larger than their expected values (>15%) could have been the result of incomplete wetting, debris within the pore, or incomplete drilling. Any of these causes would increase the efficacy of clogging after the introduction of particles. Pores with resistances much smaller than expected were rare, but when they occurred it always implied a fracture in the membrane. The final yield of functioning nanopores was approximately 25%.

## 4.2 Signal Analysis – Pore Clogging Examples

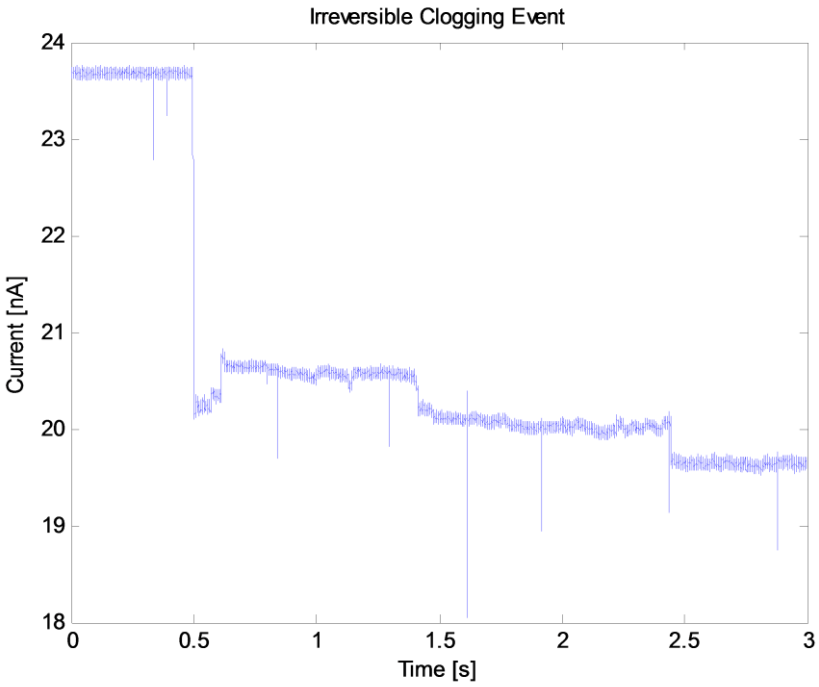


Figure 24: Irreversible Clogging Event

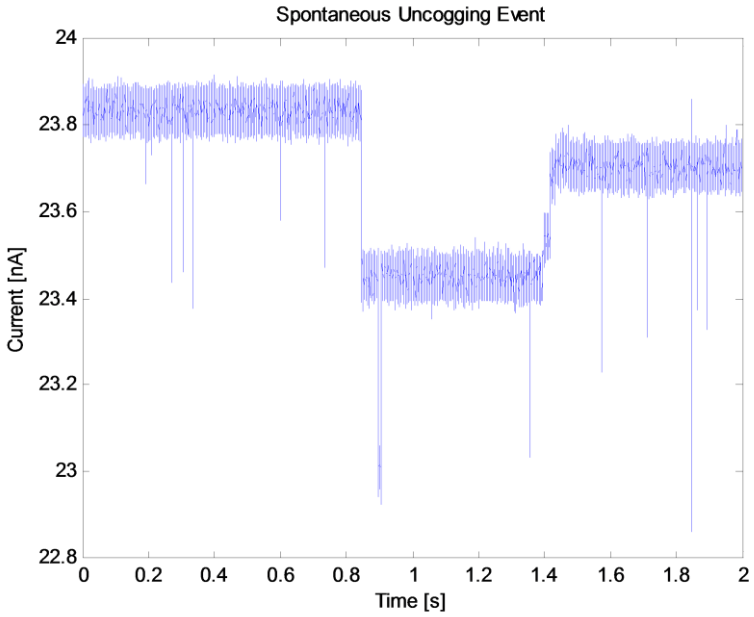


Figure 25: Spontaneous unclogging event

Figure 24 shows an example of an irreversible clogging event. In many cases, multiple discrete steps were observed until a steady current was reached. Pore resistances more than doubled after an irreversible clog. Prior to the addition of a PDMS layer to our chips, irreversibly clogged pores could be cleaned by a 4 hour soak in Piranha solution. The process usually returned the resistance to its original value and could be repeatedly used for tens of times before being accidentally fractured. However, with the inclusion of a PDMS capacitive layer, there is no apparent way of dislodging or dissolving the polystyrene particles once they have clogged the pore.

Figure 25 shows a clogging event followed by spontaneous unclogging. Throughout the duration of an experiment, several of these events occurred and have also been reported in the literature [59, 70, 74].

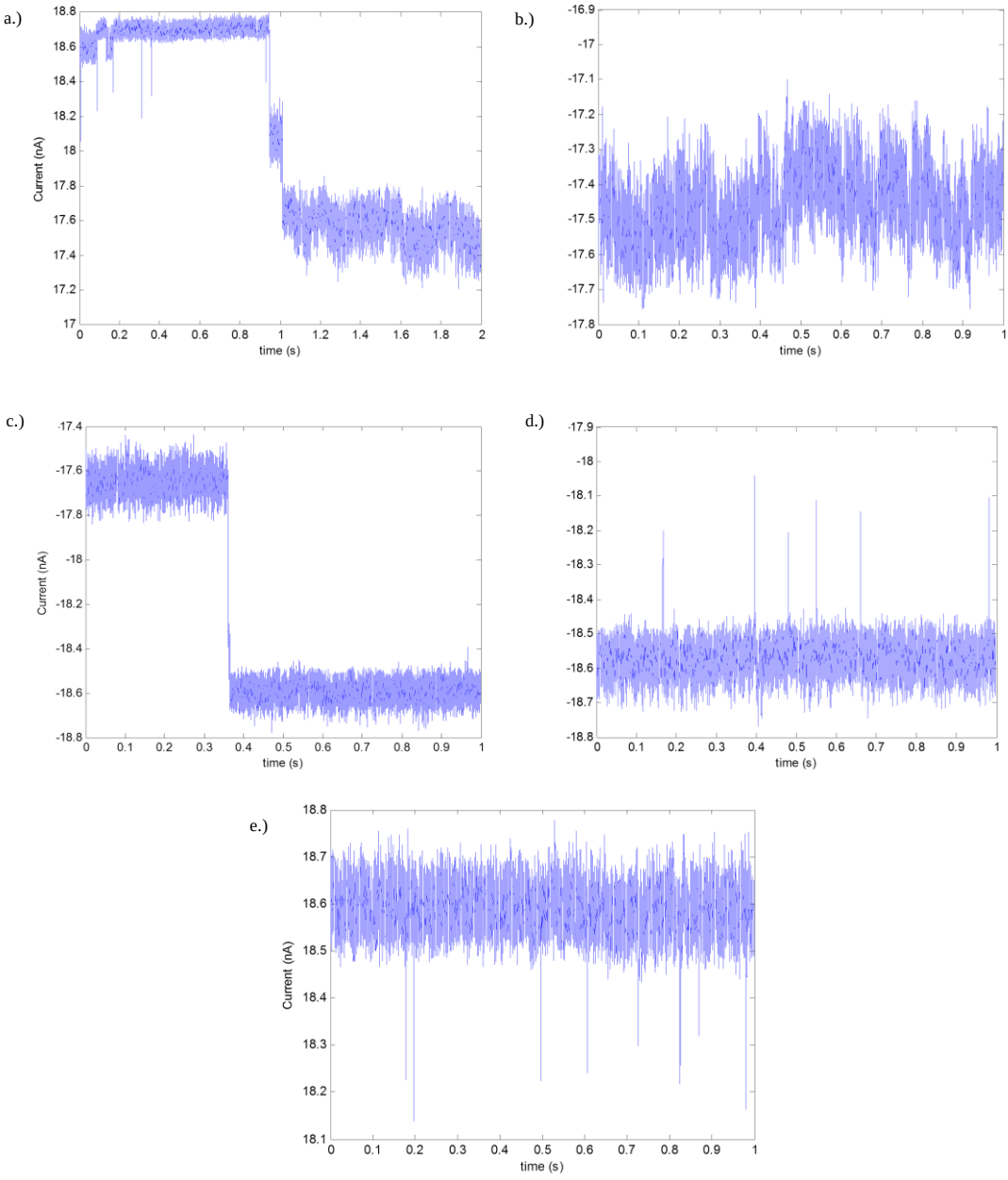


Figure 26: Unclogging of pore via reverse potential bias: a.) Clogging event b.) Reversal of potential bias c.) Removal of lodged aggregate d.) Reverse particle translocation under negative bias from trans to cis chamber e.) Return to original baseline current, particle translocation from cis to trans chambers resumes.

In a small number of chips, after a clogging event similar to that depicted in figure 25, the

particle could be dislodged from the pore by application of a large negative bias. Figures 26 show the sequence of events beginning with a step drop in baseline current, reversal of the electric potential, removal of the lodged particle(s), reverse translocation of particles in the trans chamber to the cis chamber, and finally a return to the original baseline current. It was found that a much larger negative bias (>500 mV) must be applied to remove the aggregate from the pore. In some instances, repeated switching between positive and negative voltage biases was necessary before complete unclogging occurred.

All experiments eventually ended with an irreversible clog. The duration of an experiment varied significantly from pore to pore and ranged from a few seconds to several minutes in the extreme cases.

## 4.3 Signal Analysis – Event Depths

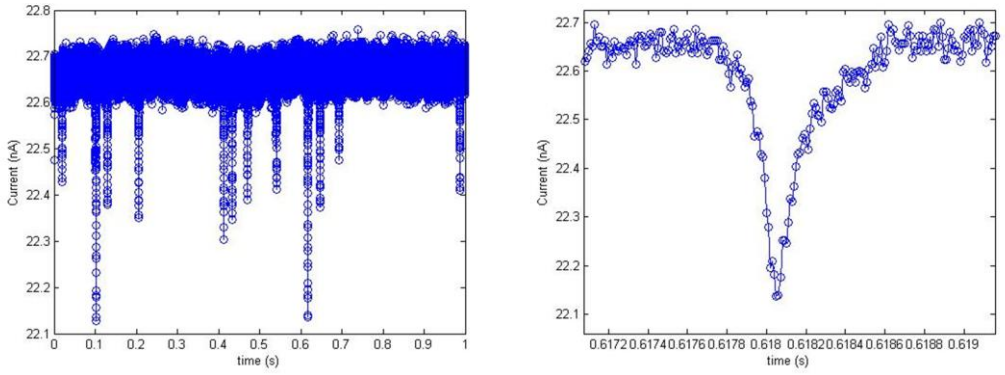


a.) b.)

Figure 27: a.) Typical particle translocation signal over a 1 second time frame b.) Expanded view of a typical particle translocation event.

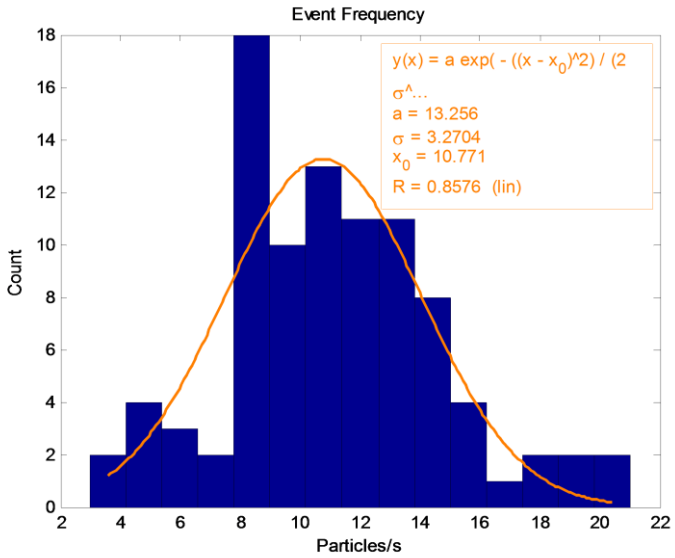


Figure 28: Typical event frequency histogram for a single experiment. Data points are added to bins based on the number of translocations in a 1 second time span.

Figure 27a shows a typical raw signal for a 1 second period of an experiment. A single particle translocation event is shown in figure 27b. Because the particles are spherical in shape, the slight asymmetry of the downward spike is evidence of a small cone angle present in the pore and results from the non-uniform velocity through the pore [74]. As mentioned previously, FIB drilled pores resemble a conical shape. While this effect was not detectable in the IV curves, the 100 nm particles act as fine resolution probes and outline the finer details of the pore geometry as they pass through them. For conservation of mass to hold, the velocity of the fluid at the entrance of the pore must be faster than at the exit where the diameter is larger. As a result, the particle velocity tends to decrease as it leaves the pore, giving rise to the slight asymmetry of the signal [74, 75].

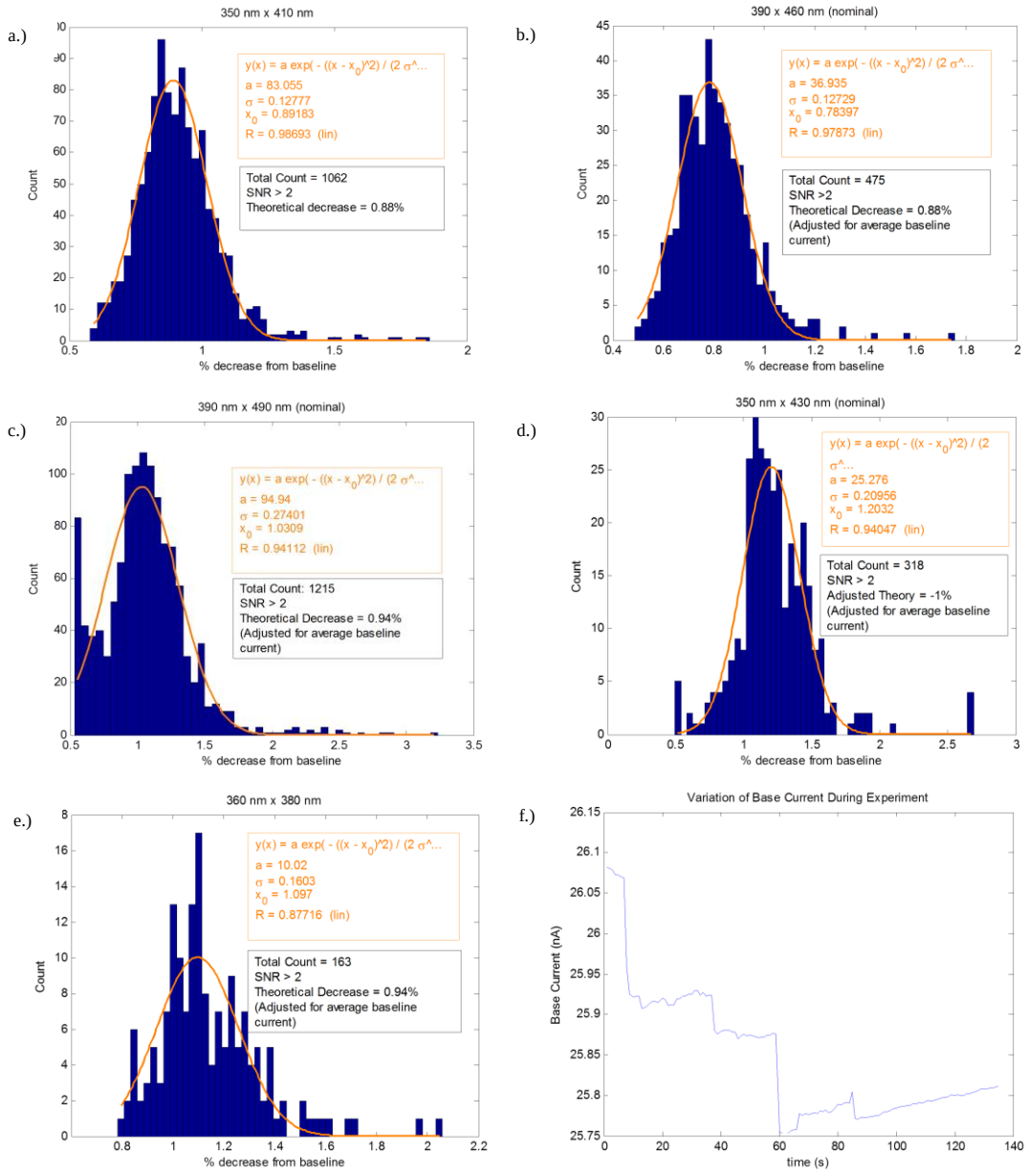


Figure 29: a.) – e.) Event depth histograms and Gaussian fits for 5 independent pores of varying diameters. A final concentration of $10^{11}$ particles/mL in 100 mM KCl were used in each test. f.) Baseline current trace as a function of time during a single experiment. Note the difference in the smaller magnitude of the current decrease and longer time frame as compared to an irreversible clog event depicted in figure 24.

The frequency of events is also comparable to the results found in Lan, et. al., for the

given concentration and are shown in figure 28.

Figures 29 show the results of 100 nm particles translocating through 5 nanopores of varying diameter. The figures show histograms of the relative decrease in current as particles pass through the pore (i.e. experimental values of equations 2.40.) Gaussian fits are overlaid in orange, and the peak of the fit occurs at the $x_o$ parameter given in the orange inset. Only current drops greater than twice the noise (>6σ of the baseline RMS current noise, SNR > 2) were included in the plots. The experimental results show good agreement with the semi-emprical formulas given in equations 2.40. The percent differences between experimental and theoretical values for plots a-e are 1.3%, 12%, 9.7%, 20%, and 16.7%, respectively. Each of these errors are within one standard deviation of the Gaussian fits.

In pores b-e, the resistance immediately increased when particles were introduced. However, the current trace did not display typical characteristics typical of an irreversible clogging event. Particle translocation events continued to occur even after the initial increase in pore resistance. In addition, the final resistances of the pores were equivalent to open pore diameters large enough for particle translocations. This could be explained by partial blockage of the pore by a single or a few nanoparticles. Furthermore, post-test inspection of the devices revealed particles gathered around the perimeter of the pore mouth, which may increase the access resistance by further disrupting the electric field lines. As shown in figure 29f, these chips also displayed a slowly decreasing baseline current as the experiment progressed, which is attributed to further accumulation of

particles near the pore. In contrast to the sharp, steep, and frequent current drops found in irreversibly clogged pores, the current change is relatively small and occurs over a much longer time frame in this case. For these pores, an adjusted pore diameter was used when calculating the theoretical current drop during particle translocation. Similar results have been seen in the works of Tsutsui [55] and Han [70]. An average baseline current for the experiment was used with the known applied potential bias to determine the pore resistance. Equation 2.17 was used to calculate a new theoretical diameter and equations 2.40 were used to calculate the expected current drop. In propagating the uncertainty from the resistance, to the uncertainty in the pore diameter, the uncertainty in the theoretical current drops for pores a-e are ±0.27%, ±0.2%, 0.24%, 0.26%, 0.28%, respectively. The uncertainty from the pore diameter (calculated to be on the order of ±1 nm) was seen to be negligible in comparison to the uncertainty in nanoparticle diameter, which had a $2\sigma$ manufacturer specified uncertainty of ±10 nm. The results of particle translocations for each pore are therefore all within their theoretical uncertainties.

The pores represented by figures d and e also show a distinct second peak at larger current drops of approximately 1.5% and 1.3%, respectively. This can be attributed to the simultaneous translocation of multiple particles. In figure 27a, two current drops are noticeably larger than the others, similar to the results of other works [57, 60] and analogous in concept to the detection of folded DNA molecules [41]. On the other end, the histogram of 29c shows a distinct peak that is lower than that of a single particle. This lower peak is not visible in the other plots because of the restriction

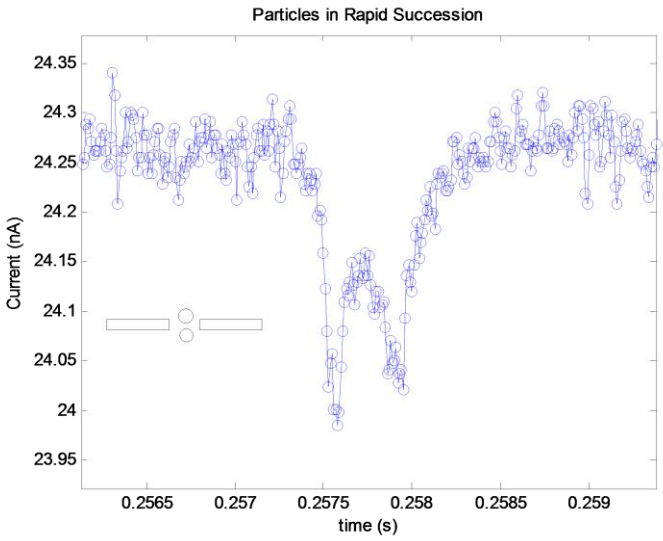


Figure 30: Current trace of two particles translocating the pore in rapid succession.

of SNR > 2. Small and short translocation signals have been attributed previously by Bacri, et. al., to nanoparticle-pore bumping [54]. In theory, particles can come into close proximity with and may sometimes collide into the membrane surface without translocating through the pore. This results from the electroosmotic flow directed outwards from the pore mouth counteracting the electrophoretic force pulling the particle towards the pore. While not actually passing through from the cis to trans chambers, these particles can still affect the device resistance up to approximately one pore diameter away resulting in relatively short and small current drops [57].

A final type of signal that was detected was that of two particles translocating in immediate succession of each other (Figure 30). This is an inherently distinct signal from a two-particle agglomerate in that instead of a single, large drop, there are two distinct

minima contained within the same translocation duration. In addition, both minima have the same magnitude and are close to the theoretical current drop that a single particle would produce. As shown in the inset, the particles are distinct and the second particle enters the pore before the first particle completely exits [57].

### 4.4 Signal Analysis – Event Durations

The event durations for the same pores in figure 29 are shown in figure 31. Theoretical velocities assume a negligible $\zeta_{pore}$ in equation 2.47 and only approximately 50% of the total voltage applied is dropped across the pore (see "Effect of access resistance" and eq. 48) [59]. Furthermore, the start and end of the signal is assumed to begin at one radial distance away from the entrance and exits of the pore [57]. Full pulse widths were used. After identification of a peak point, the start of the signal was defined as the first point to the left of the peak that was within $3\sigma$ of the baseline current, and the end of the signal was defined as the first point to the right of the peak that was within $3\sigma$ of the baseline current. The total duration of a pulse is the time between the start and end points of the event.

Pores represented by figures 27a, b, and e show a close resemblance to the predicted translocation times with percent differences of 17%, 7% and 12%, respectively. In addition, the theoretical values are all within one standard deviation from the Gaussian fit. The pore in 27c also shows a distinct peak at very short translocation times. This is in conjunction with and further supports the hypothesis of particle-pore bumping as previously described.

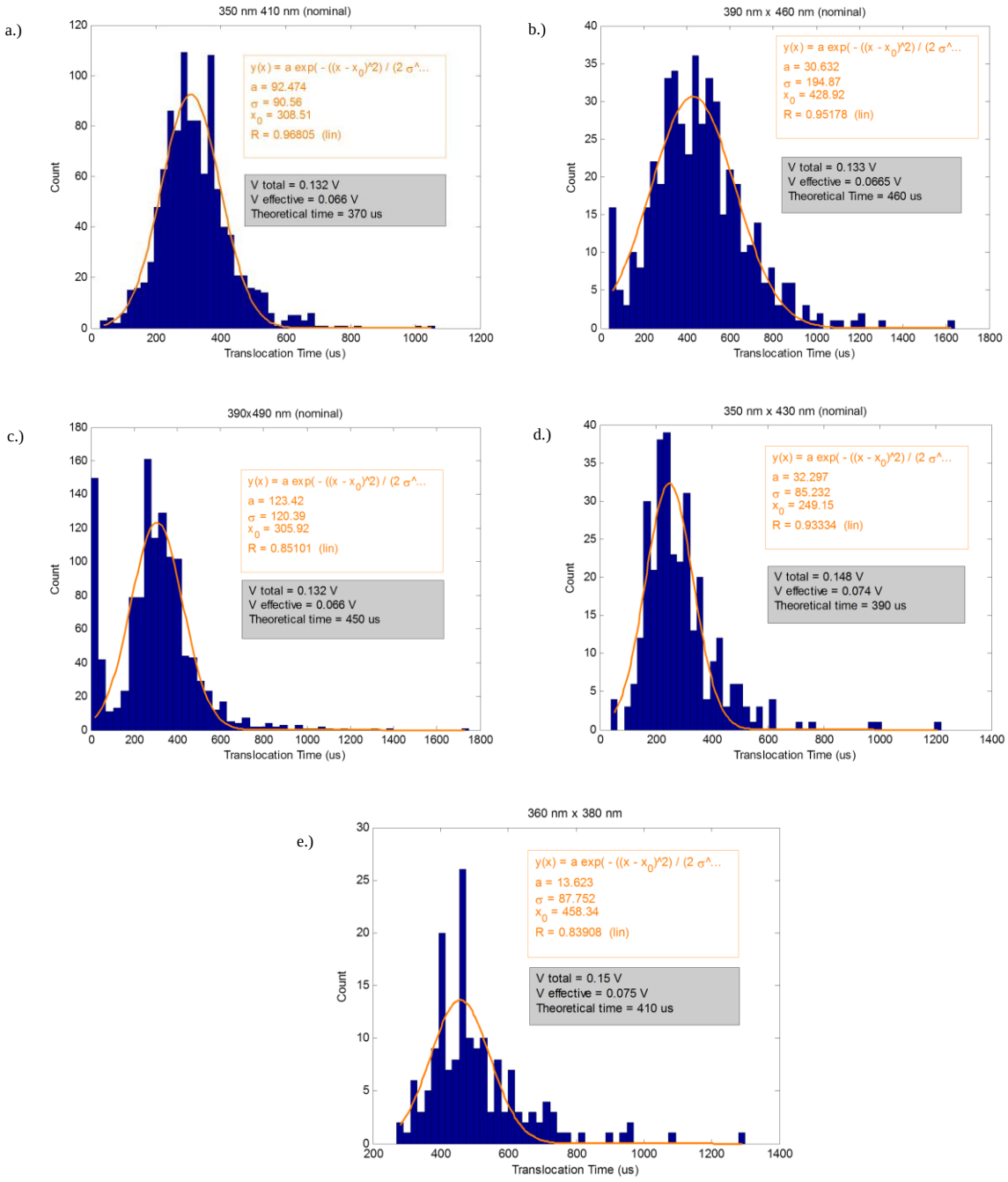


Figure 31: Particle translocation time histograms and their accompanying Gaussian fits.

While equation 2.47 offers a compact and elegant solution, it is a simplification with major assumptions. For example, particle-pore interactions are not taken into account. More accurate and precise simulations have been presented by Prabhu, Lan, and Kozak, but all are very specific to each experiment's parameters. For example, Kozak, et. al., provided numerical results for particles translocating across a pyramidal shaped pore with sharp edges (i.e. the geometry of the backside etch of the silicon wafers used in my experiments, but with the nitride membrane removed). However, as was previously discussed, resistance changes are heavily dependent on pore geometry and aspect ratio. Therefore, their results are not applicable to the pores at hand.

Another limiting factor in equation 2.47 is the ambiguity in the definition of the length over which the electric field is applied. Assuming this length is the same as the length of the sensing zone of the pore, the translocation time can be derived from equation 2.47 as:

$$t_{trans} = \frac{\eta l_{ef}^2}{\varepsilon \zeta V} \tag{4.1}$$

The length of the sensing zone, $l_{ef}$, is a debated parameter and arguably ranges from the physical length of the pore up to one pore diameter on either side of the membrane [57]. Due to its square dependence on $l_{ef}$, the theoretical translocation time used in 26a-e is unfortunately extremely sensitive to this debated parameter. The theoretical values used in the previous calculations assumed the sensing zone extended one radial distance into the solution on either side of the pore, a compromise between the two proposed extremes.

Even for a modest uncertainty in the effective pore length of $\pm \frac{1}{4}$D extensions into the fluid on either end of the pore, i.e. $l_{ef} = L \pm 2\left(\frac{1}{4}D\right)$, the uncertainties in translocation time for 26c and 26d are ± 190 us and ± 160 us, respectively. Inclusion of these uncertainties and that of the Gaussian fit shows that the theory is in good agreement with the experimental results.

Arjmandi, et. al., suggested a correction term be applied in equation 4.1 to account for the intrinsic voltage offset when the electrodes are disconnected from the external driving potential [29]:

$$t_{trans} = \frac{\eta l_{ef}^2}{\varepsilon\zeta(V+C)} \tag{4.2}$$

This intrinsic potential difference results from the difference between the electrical charge transfer of the metal electrode into the solution (i.e. dissolution of Ag/AgCl) and the electrons released into the metallic wire [76]. Although a small voltage offset was observed, unfortunately it was not recorded in the present experiments. With the given experimental conditions and Gaussian fits for each pore, the correction factor for 27a-e was calculated as 33 mV, 5 mV, 32 mV, 41 mV, -10 mV, respectively. Although exact figures were not recorded, the general offset voltage was observed to be between 1 to 2 mV. Therefore although inclusion of the correction factor C in equation 4.2 would generally increase the accuracy of the results, the uncertainty in the effective length of the sensing zone was a more significant unknown.

Without loss of generality, a more encompassing theory of particle velocities is necessary for the realization of cylindrical nanopores as ζ-potential measurement devices. While the event duration results were not as accurate as the expected current drops, they were still within uncertainty and the presented theory provides a good estimate of the speed of translocating particles and is a good starting point when determining the necessary electronic equipment specifications.

# Chapter 5: Conclusion

Nanopore sensing is a complex science involving a fundamental understanding of several engineering disciplines. A thorough guideline to producing a working nanopore system was presented in this thesis. It was found that the major difficulty was finding a middle-ground between the competing interests of noise and speed of both the electronic equipment as well as the pore-particle-electrolyte-electrode system. In turn, the experimental conditions including the correct applied potential, electrolyte concentration, nanoparticle concentration, particle to pore diameter, and noise reduction circuit elements must be chosen in accordance with the electronic system specifications.

An analysis on system noise revealed many sources of electromagnetic interferences occurring in a typical lab setting. Noise suppression was achieved in a sequential manner, addressing first the stray EM waves in the ambient by incorporation of an enclosed Faraday Cage around the pore and electrode system. Main line hum noise was addressed next, and the noisy DAQ voltage source was replaced by a quiet 9V battery and variable voltage divider circuit for precise potential control. Attention was then shifted from external sources to those inherent in the nanopore device itself. Wetting of the pore was enhanced by hydrophilicizing both surfaces with either a Piranha soak or a low-power oxygen plasma. Finally, capacitive noise reductions were achieved by coating the chip surface with a thick PDMS layer. The total noise reduction spanned three orders of magnitude from approximately ± 10 nA to a final value of ± 0.02 nA.

Particle translocation events were also difficult to achieve. Only 25% of pores with an acceptable noise level were successful in generating a steady translocation signal. Most pores experienced immediate and irreversible clogging events. Future studies must therefore focus on increasing pore yield through surface modifications conducive to translocation. In the present pores, a layer of $Al_20_3$ was included to fine-tune the final diameters. However, aluminum oxide displays a negligible surface charge in the solution used. On one hand, this assisted in particle translocation as it reduced the opposing electroosmotic flow velocity, but it also increases the probability of particle-pore interactions due to Van Der Waals forces. Surfaces with a higher ζ-potential would decrease the probability of pore clogging due to electrostatic repulsion, but would also increase the opposing flow velocity within the pore. Therefore, an in depth study of an optimal pore ζ-potential is necessary in increasing the yield of pores. The significance of increasing this yield is exacerbated by the single-use nature of each device. As such, a study to find a more robust capacitive layer than the PDMS used here is also required.

For working pores, the semi-empirical model of Davenport, et. al., produced accurate results for the magnitude of the current drop during particle translocation. Given the relatively large, manufacturer specified uncertainty in the nanoparticle diameters, the experimental signal was well within error of the theoretical model. Event durations were less accurate, however, owing to the large degree of ambiguity in the definition of the effective pore length. Given the large range of the debated extremes in $l_{ef}$, uncertainties in the theoretical velocity approached ± 40% of the total translocation time. While more

accurate simulation based models have been developed, they lack generality and are valid for particular particle-pore-electrolyte configurations. A broadly applicable semi-empirical model similar to that of Davenport, et al., used for event depths is necessary before nanopores can be used to accurately and reliably determine the ζ-potential of particles.

Nanopore models to determine the shape and geometry of nanoparticles have not been as thoroughly explored as those for size and ζ-potential. While long strands of DNA have been modeled as cylindrical particles, other geometries have not been explored or simulated. A goal in the immediate future is therefore to pass particles of similar size, but different geometry and to determine the ability of these sensors to differentiate between them. This is a relatively new venture in the extension of the applicability of pore sensors and promises to have a large impact on the characterization of nanoparticles for use as drug delivery agents.

# References


[1] W. Chan, *Bio-Applications of Nanoparticles*. vol. 620; Landes Bioscience and Springer Science+Business Media, LLC: 2007.

[2] G. Schmid, *Nanoparticles: From Theory to Application*.; Wiley-VCH: 2005.

[3] S. McNeil, *Characterization of Nanoparticles Intended for Drug Delivery*, vol. 697; Springer Science+Business Media, LLC: 2011.

[4] The American Cermaic Society, *Progress in Nanotechnology: Applications*; John Wiley & Sons. Inc.: 2010.

[5] M. Arruebo, R. Fernandez-Pacheco, M. R. Ibarra, and J. Santamaria, "Magnetic nanoparticles for drug delivery," *Nano Today*, vol. 2, no. 3, pp. 22-32, 2007.

[6] R. Singh, and J. Lillard, "Nanoparticle-based targeted drug delivery," *Experimental and Molecular Pathology*, vol. 86, no. 3, pp. 215-223, 2009.

[7] R.B. Gupta, and U.B. Kompella, *Nanoparticle Technology for Drug Delivery*; Informa Healthcare: 2006.

[8] M. Hamidi, A. Azadi, and P. Rafiei, "Hydrogel nanoparticles in drug delivery," *Advanced drug delivery reviews*, vol. 60, no. 15, pp. 1638-1649, 2008.

[9] A. Wang, R. Langer, and O. Farokhzad, "Nanoparticle delivery of cancer drugs," *Annual review of medicine*, vol. 63, pp. 185-198, 2012.

[10] R. Agarwal, V. Singh, P. Jurney, L. Shi, S.V. Sreenivasan, and R. Krishnendu, "Mamallian cells preferentially internalize hydrogel nanodiscs over nanorods and use shape-specific uptake mechanisms," *PNAS*, vol. 110, no. 43, pp. 17247-17252, 2013.

[11] V. Torchilin, "Tumor delivery of macromolecular drugs based on the EPR effect," *Advanced drug delivery reviews*, vol. 63, no. 3, pp. 131-135, 2011.

[12] T. Ito, L. Sun, M. A. Bevan, and R. Crooks, "Comparison of nanoparticle size and electrophoretic mobility measurements using a carbon-nanotube-based coulter counter, dynamic light scattering, transmission electron microscopy, and phase analysis light scattering," *Langmuir*, vol. 20, no. 16, pp. 6940-6945, 2004.

[13] T. Ito, L. Sun, R.R. Henriquez, and R. M. Crooks, "A carbon nanotube-based coulter nanoparticle counter," Accounts of chemical research, vol. 37, no. 12, pp. 937-945, 2004.

[14] J. Wang, J. Ma, Z. Ni, L. Zhang, and G. Hu, "Effects of access resistance on the resistive pulse caused by a translocating of a nanoparticle through a nanopore," *RSC Advances*, vol. 4, no. 15, pp. 7601-7610, 2014.

[15] V.A. Hackley, and J.D. Clogston, "Measuring the Hydrodynamic Size of Nanopaticles in Aqueous Media Using Batch-Mode Dynamic Light Scattering," *Characterization of Nanoparticles Intended for Drug Delivery Methods in Molecular Biology*, vol. 697, pp. 35-52, 2011.

[16] C. Zhang, J.W. Chung, and R. Priestly, "Dialysis nanoprecipitation of polystyrene nanoparticles," *Macromolecular rapid communications*, vol. 33, no. 20, pp. 1798-1803, 2012.

[17] C. Zhang, V. Pansare, R. K. Prud'homme, and R. Priestly, "Flash nanoprecipitation of polystyrene nanoparticles," *Soft Matter*, vol. 8, no. 1, pp. 86-93, 2011.

[18] M. Firnkes, D. Pedone, J. Knezevic, M. Doblinger, and U. Rant, "Electrically facilitated translocations of proteins through silicon nitride nanopores: conjoint competitive action of diffusion, electrophoresis and electroosmosis" *Nano Letters*, vol. 10, no. 6, pp. 2162-2167, 2010.

[19] G. Goyal, K. Freedman, and M. J. Kim, "Gold nanoparticle translocation dynamics and electrical detection of single particle diffusion using solid-state nanopores," *Analytical chemistry*, vol. 85, no. 17, pp 8180, 2013.

[20] O. Lemine, "Microcstructural characterization of alpha FE2O3 nanoparticles using, XRD line profile analysis, FE-SEM, and FT-IR," *Superlattices and microstructures*, vol. 45, no. 6, pp. 576-582, 2009.

[21] N. Fukuhara, K. Suzuki, and Y. Nihei, "Characterization of environmental nanoparticles," *Applied Surface Science*, vol. 255, no. 4, pp. 1538-1540, 2008.

[22] J. Grobelny, F. W. DelRio, N. Pradeep, D. Kim. V. Hackley, and R. Cook, "Size measurement of nanoparticles using atomic force microscopy," *Methods in molecular biology*, vol. 697, pp. 71, 2011.

[23] Y. Gu, H. Xie, J. Gao, D. Liu, C. Williams, and C. Murphy, "AFM characterization of dendrimer-stabilized platinum nanoparticles," *Langmuir*, vol. 21, no. 7, pp. 3121-3131, 2005.

[24] V. Diculescu, A. Chiorcea-Paquim, O. Corduneanu, A. Oliveira-Brett, " Palladium nanoparticles and nanowires desposited electrochemically: AFM and electrochemical characterization," *Journal of Solid State Electrochemistry*, vol. 11, no. 7, pp. 887-898, 2007.

[25] S. Howorka, and Z. S. Siwy, "Nanopores as protein sensors," *Nature biotechnology*, vol. 30, no. 6, pp. 506-507, 2012.

[26] W.H. Coulter, "Means for counting particle suspended in a fluid," U.S Patent 2,656,598, 1953.

[27] S.M. Iqbal, R. Bashir, *Nanopores: Sensing and Fundamental Biological Interactions*; Springer: 2011.

[28] D. Kozak, W. Anderson, R. Vogel, S. Chen, F. Antaw, and M. Trau, "Simultaneous Size and zeta-Potential Measurements of Individual Nanoparticles in Dispersion Using Size-Tunable Pore Sensors," *ACS Nano*, vol. 6, no. 8, pp. 6690-6997, 2012.

[29] N. Arjmandi, W. Van Roy, L. Lagae, and G. Borghs, "Measuring the electric charge and zeta potential of nanometer-sized objects using pyramidal-shaped nanopores," *Analytical chemistry*, vol. 84, no. 20, pp. 8490-8496, 2012.

[30] R. Xu, "Zeta Potential Determination of Colloidal Particles," Presentation at the Co-Nanomet Workshop, 2010.

[31] M. Davenport, K. Healy, M. Pevarnik, N. Teslich, S. Cabrini, and A. Morrison, "The role of pore geometry in single nanoparticle detection," *ACS Nano*, vol. 6, no. 9, pp. 8366-8380, 2012.

[32] A. Han, M. Creus, G. Schurmann, V. Linder, T.R. Ward, and N.F. de Rooij, "Label-free detection of single protein molecules and protein-protein interactions using synthetic nanopores," *Analytical Chemistry*, vol. 80, no. 12, pp. 4651-4658, 2008.

[33] B.M. Venkatesan, A.B. Shah, J.M. Zuo, and R. Bashir, "DNA Sensing Using Nanocrystalline Surface-Enhanced Al2O3 Nanopore Sensors," *Advanced Functional Materials*, vol. 20, no. 8, pp. 1266-1275, 2010.

[34] B.M. Venkatesan, D. Estrada, S. Banerjee, X. Jin, V. Dorgan, M.H Bae, N.R. Aluru, E. Pop, R. Bashir, "Stacked Graphene-Al2O3 Nanopore Sensors for Sensitive Detection of DNA and DNA-Protein Complexes," *ACS Nano*, vol. 6, no. 1, pp. 441-450, 2012.

[35] M. Zwolak, and M. Di Ventra, "Electronic signature of DNA nucleotides via transverse transport," *Nano Letters*, vol. 5, no. 3, pp. 421-424, 2005.

[36] H. Postma, "Rapid sequencing of individual DNA molecules in graphene nanogaps," *Nano Letters*, vol. 10, no. 2, pp. 420-425, 2010.

[37] A.P. Ivanov, E. Instuli, C.M. McGilvery, G. Baldwin, D. McComb, and T. Albrecht, " DNA tunneling detector embedded in a nanopore," *Nano Letters*, vol. 11, no. 1, pp. 279-285, 2011.

[38] N. Mohanty, and V. Berry, "Graphene-based single-bacterium resolution biodevice and DNA transistor: interfacing graphene derivatives with nanoscale and microscale biocomponents," *Nano Letters*, vol. 8, no. 12, 2008.

[39] S.M. Avdoshenko, D. Nozaki, C. Gomes da Rocha, J.W. Gonzalez, M. Lee, and R. Gutierrez, "Dynamic and electronic transport properties of DNA translocation through graphene nanopores," *Nano Letters*, vol. 13, no. 5, pp. 1969-1976, 2013.

[40] J. Clarke, H.C. Wu, L. Jayasinghe, A. Patel, S. Reid, and H. Bayley, "Continuous base identification for single-molecule nanopore DNA sequencing," *Nature Nanotechnology*, vol. 4, no. 4, pp. 265-270.

[41] J.B. Edel, and T. Albrecht, *Engineered Nanopores for Bioanalytical Applications*; Elsevier, Inc.: 2013.

[42] W.J. Lan, D.A. Holden, and H.S. White, "Pressure-Driven Nanoparticle Transport across Glass Membranes Containing a Conical-Shaped Nanopore," *Journal of Physical Chemistry*, vol. 115, no. 38, pp. 18445-18452.

[43] V. Zeghbroeck, Principles of semiconductor devices; Online Textbook (accessed April 25, 2014.

[44] *A Simple Derivation of the Nernst Equation.* [Online]. http://www.columbia.edu/cu/biology/courses/w3004/Nernstequationderiv.pdf (accessed April 9, 2014).

[45] B. Hille, "Pharmacological modifications of the sodium channels of frog nerve," *The Journal of general physiology*, vol. 51, no. 2, pp. 199-219.

[46] J.E. Hall, "Access resistance of a small circular pore," *The Journal of general physiology*, vol. 66, no. 4, pp. 531-532.

[47] G. Itzel, and C. Darnault, "Aggregation and transport of nano-TiO2 saturated porous media: Effects of pH, surfactants and flow velocity," *Water Research*, vol. 45, no. 2, pp 839-851.

[48] W. Norde , *Colloids and interfaces in life sciences*, 2nd ed.; CRC Press: 2011.

[49] P. Tabeling, *Introduction to Microfluidics*; Oxford University Press: 2010.

[50] V. Bagotsky, *Fundamentals of Electrochemistry*, 2nd ed.; Wiley: 2005.

[51] C. Ho, R. Qiao, J.B. Heng, A. Chatterjee, G. Timp, R.J. Timp, N. Aluru, and K. Hess, "Electrolytic Transport through a Synthetic Nanometer-Diameter Pore,"

*Proceedings of the National Academy of Sciences of the United States of America*, vol. 102, no. 30, pp. 10445-10450, 2005.

[52] J. Maxwell, "A treatise on electricity and magnetism," vol. 1, 3rd ed., Oxford: Clarendon, 1904.

[53] R.W. DeBlois, and C.P. Bean, "Counting and sizing of submicron particles by the resistive pulse technique," *Review of Scientific Instruments*, vol. 79, no. 7, pp. 909-916, 1970.

[54] L. Bacri, A.G. Oukhaled, B. Schiedt, G. Patriarche, E. Bourhis, and J. Gierak, "Dynamics of colloids in single soild-state nanopores," *The journal of physical chemistry*, vol. 115, no. 12, pp. 2890-2898.

[55] M. Tsutsui, Y. Maeda, Y. He, S. Hongo, S. Ryuzaki, S. Kawano, T. Kawai and M. Taniguchi, "Trapping and identifying single-nanoparticles using a low-aspect ratio nanopore," *Applied Physics Letters*, vol. 103, no. 1, pp. 013108-0131085, 2013.

[56] D. Hoogerheide, S. Garaj, and J. Golovchenko, "Probing surface charge fluctuations with solid-state nanopores," *Physical review letters*, vol. 102, no. 25, pp. 256804, 2009.

[57] A. Prabhu, T. Jubrey, K. Freedman, R. Mulero, P. Dutta, M.J. Kim, "Chemically modified solid-state nanopores for high throughput nanoparticle separation," *Journal of physics*, vol. 22, no. 45, pp. 454107.

[58] Molecular Devices, *The Axon Guide: A Guide to Electrophyisiology & Biophysics Laboratory Techniques*, 3rd ed.; MDS Analytical Technologies: 2008.

[59] P. Chen, D.B. Farmer, J. Golovchenko, R.G. Gordon, D. Branton, "Atomic layer deposition to fine-tune the surface properties and diameters of fabricated nanopores," *Nano Letters*, vol. 4, no. 7, pp. 1333-1337, 2004.

[60] J.L. Kong, H.W. Wu, L.P. Liu, X. Xie, X.F. Ye, and Q.J. Liu, "Silicon Nitride Nanopores for Nanoparticle Sensing," *Journal of Nanoscience and Nanotechnology*, vol. 13, no. 6, pp. 4010-4016, 2013.

[61] J.D. Uram, K. Ke, and M. Mayer, "Noise and bandwidth of current recordings from submicrometer pores and nanopores," *ACS Nano*, vol. 2, no. 5, pp. 857-872, 2008.

[62] R.M.M. Smeets, U.F. Keyser, N.H. Dekker, and C. Dekker, "Noise in solid-state nanopores," *Proceedings of the National Academy of Sciences of the United States of America*, vol. 105, no. 2, pp. 417-421, 2008.

[63] V. Dimitrov, G. Timp, U. Mirsaidov, D. Wang, T. Sorsch, W. Mansfield, J. Miner, F. Klemens, R. Cirelli, and S. Yemenicioglu, " Nanopores in solid-state membranes

engineered for single molecule detection," *Nanotechnology*, vol. 21, no. 6, p. 065502, 2010.

[64] Z. Zhang, J. Zhe, S. Chandra, and J. Hu, "An electronic pollen detection method using Coulter counting principle," *Atmospheric Environment*, vol. 39, no. 30, pp. 5446-5453, 2005.

[65] V. Tabard-Cossa, D. Trivedi, M. Wiggin, N.N. Jeta, and A. Marziali, "Noise analysis and reduction in solid-state nanopores," *Nanotechnology*, vol. 18, no. 30, p. 305505, 2007.

[66] M. Ayub, A. Ivanov, J. Hong, P. Kuhn, E. Instuli, J.B. Edel, T. Albrecht, "Precise electrochemical fabrication of sub-20 nm solid-state nanopores for single-molecule biosensing," *J. Phys. Condens. Matter*, vol. 22, no. 45, 2010.

[67] E. Beamish, H. Kwok, V. Tabard-Cossa, and M. Godin, "Precise control of the size and noise of solid-state nanopores using high electric fields," *Nanotechnology*, vol. 23, no. 40, p. 405301, 2012.

[68] S.M. Bezrukov, M. Winterhalter, "Examining noise sources at the single-molecule level: 1/f noise of an open maltoporin channel," *Physical Review Letters*, vol. 85, no. 1, pp. 202-205, 2000.

[69] F.N. Hooge, "1/f Noise sources," *IEEE Transactions on Electron Devices*, vol. 41, no. 11, pp. 1926-1935, 1994.

[70] A. Han, G. Schurmann, G. Mondin, R.A. Roland, N.G. Hegelbach, N. de Rooij, and U. Staufer, "Sensing protein moelcules using nanofabricated pores," *Applied Physics Letters*, vol. 75, no. 9, pp. 093901-093901-3, 2006.

[71] S. Handy, *Applications of Ionic Liquids in Science and Technology*; InTech: 2011.

[72] E.C. Yusko, R. An, M. Mayer, "Electroosmotic flow can generate ion current rectification in nano- and micropores," *ACS Nano*, vol. 4, no. 1, pp. 477-487, 2010.

[73] M.L. Kovarik, K. Zhou, S.C. Jacobson, "Effect of conical nanopore diameter on ion current rectification," *The journal of physical chemistry*, vol. 113, no. 49, pp. 15960-15966, 2009.

[74] W.J. Lan, and H. White, "Diffusional motion of a particle translocating through a nanopore," *ACS Nano*, vol. 6, no. 2, pp. 1757-1765, 2012.

[75] W.J. Lan, D. Holden, B. Zhang, and H.S White, "Nanoparticle transport in conical-shaped nanopores," *Analytical chemistry*, vol. 83, no. 10, pp. 3840-3847, 2011.

[76] E. Niedermeyer, and F.L. Da Silva, *Electroencephalography: Basic Principles, Clinical Applications, and Related Fields*, 5th ed.; Lippincott Williams & Wilkins: 2005.

[77] *Zeta Potential*. [Online]. http://en.wikipedia.org/wiki/Zeta_potential (accessed on January 3rd, 2014).